catalysts

Review

Recent Advances in Coke Management for Dry Reforming of Methane over Ni-Based Catalysts

Zhenchao Xu [1] and Eun Duck Park [1,2,*]

[1] Department of Energy Systems Research, Ajou University, 206, World cup-ro, Yeongtong-Gu, Suwon 16499, Republic of Korea; zhenchao@ajou.ac.kr
[2] Department of Chemical Engineering, Ajou University, 206, World cup-ro, Yeongtong-Gu, Suwon 16499, Republic of Korea
* Correspondence: edpark@ajou.ac.kr

Abstract: The dry reforming of methane (DRM) is a promising method for controlling greenhouse gas emissions by converting CO_2 and CH_4 into syngas, a mixture of CO and H_2. Ni-based catalysts have been intensively investigated for their use in the DRM. However, they are limited by the formation of carbonaceous materials on their surfaces. In this review, we explore carbon-induced catalyst deactivation mechanisms and summarize the recent research progress in controlling and mitigating carbon deposition by developing coke-resistant Ni-based catalysts. This review emphasizes the significance of support, alloy, and catalyst structural strategies, and the importance of comprehending the interactions between catalyst components to achieve improved catalytic performance and stability.

Keywords: methane; carbon dioxide; dry reforming; coke resistance; nickel; syngas

Citation: Xu, Z.; Park, E.D. Recent Advances in Coke Management for Dry Reforming of Methane over Ni-Based Catalysts. *Catalysts* **2024**, *14*, 176. https://doi.org/10.3390/catal14030176

Academic Editors: Cheng Zhang, Huixiang Li and Ping Lu

Received: 2 February 2024
Revised: 20 February 2024
Accepted: 27 February 2024
Published: 1 March 2024

1. Introduction

The rising energy demand owing to the continued growth of the global economy has led to rapid advances in energy technology [1,2]. Despite the apparent advantages of renewable energy sources in terms of environmental sustainability, fossil fuels such as coal, oil, and natural gas dominate global energy production and are expected to maintain their prominence for some time [3]. Therefore, mitigating the adverse environmental effects of burning fossil fuels and managing carbon dioxide (CO_2) emissions are pertinent [4–8].

Methane (CH_4), the main component of natural gas, is widely utilized as a fuel owing to its high calorific value [9]. However, given that methane has the highest hydrogen-to-carbon ratio among the hydrocarbons, it is desirable for use as a chemical raw material rather than simply as a fuel [10–15]. In this regard, research and development in the field of the dry reforming of methane (DRM) has garnered considerable attention [16–19]. This innovative process offers a promising pathway for transforming CH_4 into high value-added products, thereby mitigating its environmental impact and maximizing its potential as a valuable resource. The process involves the reaction of CH_4 with CO_2, resulting in the production of a syngas composed of CO and H_2 with a H_2/CO molar ratio of one (Equation (1)), which offers potential for specific downstream processes such as hydroformylation and Fischer–Tropsch synthesis for the production of liquid fuels as a solution to the storage and transportation challenges inherent in the use of gaseous fuels [20].

$$CH_4 + CO_2 \leftrightarrow 2CO + 2H_2 \ \Delta H^0_{298K} = 247.3\ \text{kJ/mol} \tag{1}$$

The concept of the DRM was initially conceived to utilize the CO_2 present in natural gas wells and biogas because of its unique ability to convert waste gases into chemicals without the need for costly and time-consuming CO_2 separation and purification processes [21,22]. The DRM is a prime example of a highly endothermic reaction where both reactants, CO_2 and CH_4, have stable chemical properties owing to the strong bond strengths of C=O and C-H and their respective stable molecular configurations. Therefore, achieving high yields of H_2 and CO typically requires elevated reaction temperatures (typically > 750 °C), causing significant energy consumption and subsequent increase in operational costs. [23]. Furthermore, during the DRM process, a reverse water–gas shift (RWGS) reaction may occur in parallel (Equation (2)), leading to the consumption of H_2 and a decrease in the H_2/CO ratio to a value below one. Even though the H_2 yield will decrease, its influence on the sustainability of the DRM is not deemed significant. However, effective measures to suppress or prevent the occurrence of the RWGS by modifying the reaction temperature can be implemented [24]. Additionally, the use of membrane reactors to separate H_2 and the quenching of the product gas can be employed to mitigate the effects of a RWGS [25,26].

$$\mathrm{CO_2 + H_2 \leftrightarrow CO + H_2O}\ \Delta H^0_{298K} = 41.0\ \mathrm{kJ/mol} \tag{2}$$

The most critical concern in the catalytic process is the formation of carbon, mainly through the CH_4 cracking (Equation (3)) and Boudouard reaction (Equation (4)) pathways, which may result in the loss of catalytic activity and ultimately shorten the lifespan of the catalyst, thereby limiting its application in industrial DRM processes.

$$\mathrm{CH_4 \leftrightarrow C + 2H_2}\ \Delta H^0_{298K} = 75.0\ \mathrm{kJ/mol} \tag{3}$$

$$\mathrm{2CO \leftrightarrow C + CO_2}\ \Delta H^0_{298K} = -173.0\ \mathrm{kJ/mol} \tag{4}$$

In recent decades, DRM reactions have been extensively studied to identify solutions for the catalyst deactivation due to carbon deposition. This problem has long been a topic of interest among researchers working to develop effective strategies for mitigating catalyst deactivation and extending the catalyst lifetime [27–31]. The results of these studies have revealed the mechanisms underlying the carbon deposition process and helped identify potential methods for preventing or mitigating catalyst deactivation. Overall, assessing effective solutions for the catalyst deactivation in DRM reactions is a constant and essential area of research.

In this review, we aimed to organize and summarize various carbon management strategies related to preventing catalyst deactivation in the DRM that have been developed in recent years. Starting from the mechanism of catalyst coking, we focus on analyzing optimization strategies for anti-coking catalysts. By reviewing the state-of-the-art literature on this topic, we aim to contribute to the field of catalysis by providing insights into potential strategies to mitigate catalyst deactivation and improve the performance of the DRM, with an emphasis on both academic and practical applications.

2. Mechanism of Coke Formation

DRM technology is still considered immature owing to catalyst deactivation issues. The endothermic nature of the DRM inevitably leads to coking and carbon deposition at high reaction temperatures, which can attack the active metal sites, acidic sites, basic sites, and radical-mediated sites of catalysts, or cover the catalyst surface to prevent the adsorption of the reaction gas on the catalyst surface, thus severely affecting the catalyst performance and lifetime. Typically, the catalysts employed in DRM reactions are predominantly metal-based supported catalysts, and the impact of carbon or coke on their functionality has been elucidated, as shown in Figure 1 [32]. First, the adsorption of carbon can manifest in various ways, including in a strong chemisorption as a monolayer and physical adsorption in multiple layers. In either scenario, the presence of carbon can obstruct the accessibility of reactants to the metal surface sites.

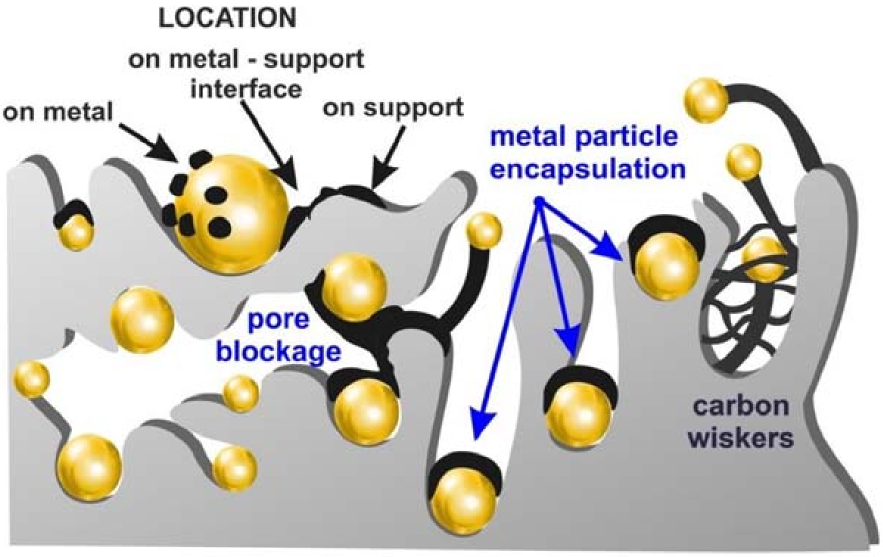

Figure 1. Formation of a coke deposit on a catalyst surface [32]. Copyright 2021, with permission from MDPI.

Additionally, carbon may entirely encapsulate the metal particles, leading to complete deactivation. Furthermore, micropores and mesopores are prone to clogging with carbon, making them inaccessible to reactants. In certain instances, the accumulation of robust carbon filaments in pores can exert sufficient pressure to cause the support material to fracture, leading to the disintegration of the catalyst pellets and plugging of the reactor voids. In this case, the irreversible deterioration of the catalyst bed owing to fouling and the attrition/crushing mechanism results in catalyst deactivation, thereby necessitating catalyst replacement.

In the DRM, the carbon in coke may originate from the reactant gases or products, including CH_4 and CO. The coke formation pathways associated with these gases are briefly discussed below. Figure 2 shows a schematic of the carbon formation and removal reactions on the catalyst surface [33].

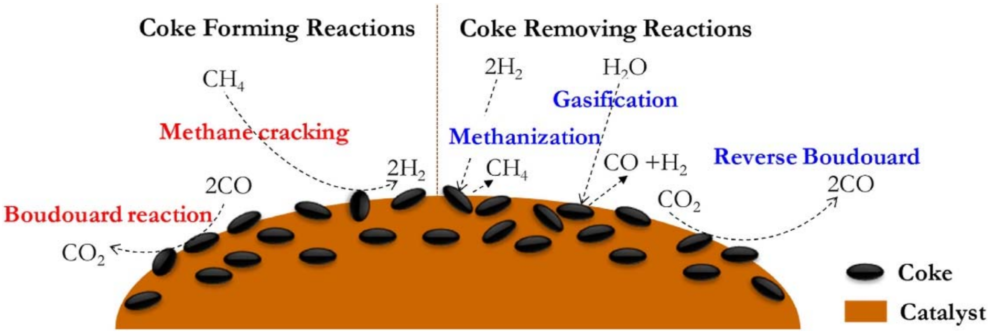

Figure 2. Carbon-forming and -removing reactions under the CO_2 reforming of methane [33]. Copyright 2022, with permission from Elsevier.

2.1. Deep Methane Cracking

The deep cracking of CH_4 is one of the significant factors contributing to catalyst carbon deposition; CH_4 can be broken down into one carbon and two H_2. Although the non-catalytic thermal cracking of CH_4 is thermodynamically unfavorable and typically requires temperatures exceeding 1000 °C, introducing a catalyst, specifically under DRM reaction conditions, significantly lowers the temperature limit for deep CH_4 cracking [34]. For instance, when using Ni-based catalysts, it can occur at temperatures as low as 500 °C [34]. Therefore, developing strategies for manipulating the reaction parameters to control coke formation is necessary. Several strategies have been proposed, such as utilizing CO_2 or

H_2 to gasify the carbon deposited on the catalyst, thereby regenerating the catalyst [35,36]. Moreover, the efficiency of carbon gasification can be significantly improved by enhancing the physicochemical properties of the catalyst, such as increasing the mobility of lattice oxygen ions and surface oxygen vacancies over Ni catalysts supported on ceria [37].

2.2. Carbon Monoxide Disproportionation

CO undergoes a cleavage to form C* and CO_2 during the CO disproportionation process so that C* blocks the active sites and decreases the efficiency of the catalyst over time [28]. In the case of nickel-based catalysts, the dissociation of CO typically occurs between 520 and 800 °C. Initially, CO was adsorbed onto the surface of the nickel (Ni) particles, forming substoichiometric nickel carbide and carbon dioxide [36]. The unstable nature of nickel carbide as a reaction intermediate leads to further decomposition, resulting in the formation of carbon and its deposition on the Ni surface, causing catalyst deactivation [37].

According to Bartholomew [38,39], the carbon resulting from CO disproportionation can be classified into various types, including C_α: adsorbed atomic carbon bounding with metallic centers, showing the most reactive (dispersed, surface carbide), C_β: amorphous carbon, which result from the polymerization of C_α, C_v: vermicular carbon, which is partially hydrogenated and exists in the form of carbon–carbon chains, which imparts lower reactivity compared to amorphous carbon, and C_c: graphitic carbon, consisting of six-carbon ring compounds which are least reactive. Some of these can be transformed into others. For instance, C_α transforms into C_β at temperatures above 325 °C, and C_β transforms into C_c at even higher temperatures [39]. The formation of diverse deposited carbon is governed by the temperature and reaction time and the parameters of the catalyst, including the location, concentration, and size of the active metal, as well as the type of active metal, support/promoter, and surface area of the support [40–46]. Moreover, they form at different temperatures and exhibit different peak temperatures for their reaction with H_2, resulting in varied impacts on catalyst deactivation. The deactivation rate (r_d) is measured by identifying the difference in the rate of coke or carbon formation (r_f) and gasification (r_g), i.e., $r_d = r_f - r_g$. Carbon or coke precipitates when the production rate of the carbon precursor exceeds the gasification rate ($r_f > r_g$). Accordingly, catalyst deactivation via carbon or coke formation is circumvented in the temperature regions where the formation rate is lower than that of the gasification [47].

Although the formation of coke deposits can potentially lead to the deactivation or disintegration of the catalyst material, carbon deposition is not without its benefits. Pechimuthu et al. [48] have redefined the role of deposited carbon in the DRM. They observed a steady state involving carbon deposition and consumption, indicating that the one-dimensional carbon nanotubes deposited on the surface of the Ni catalyst may serve as reaction intermediates generated during the DRM process (Figure 3). These intermediates react with CO_2 to remove it and contribute to the yield of the DRM by generating CO. Furthermore, microkinetic modeling has demonstrated that as the coverage of carbon on the surface of Ni-based catalysts increases, surface reconstruction leads to the formation of a steady-state Ni-C surface structure [49]. The unique carbon-based Mars–van Krevelen mechanism of the Ni-C surface structure exhibited a higher reaction activity and turnover frequency than the surface reaction mechanism, resulting in a higher catalytic activity and more optimized resistance to carbon deposition. Moreover, Chen et al. [50] developed a carbide-based Ni@C/MCM-750 catalyst where the carbon layer acted as a protective shell, shielding small Ni particles from reaction-induced restructuring, aggregation, and coking.

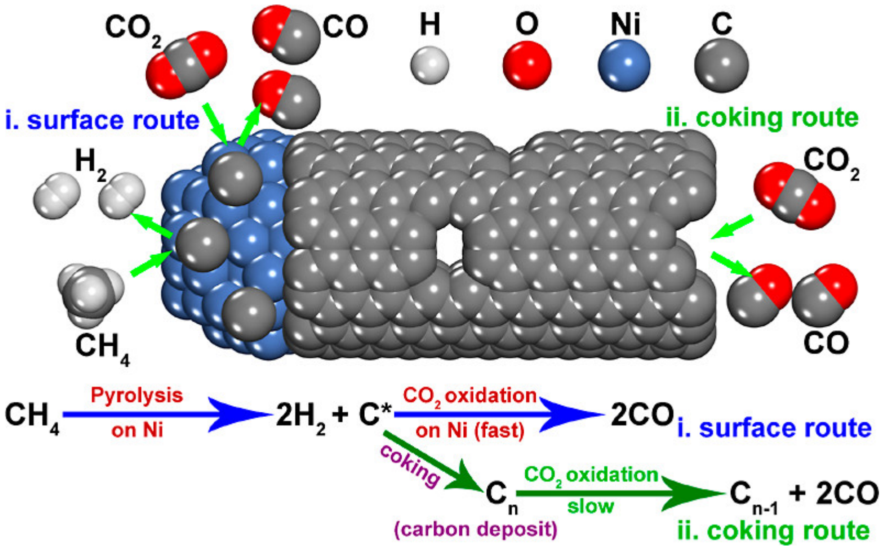

Figure 3. Schematic of the DRM reaction mechanism showing two different routes. The first route (i) is the typically envisioned surface catalytic reaction, whereas the second route (ii) involves the formation and oxidation of coke to produce CO [48]. Copyright 2022, with permission from the American Chemical Society.

3. Design Strategies for Coke-Resistant Catalysts

3.1. Effect of Support

The physicochemical properties of the catalyst support play a crucial role in determining the form of the active component precursor, as well as the activity, selectivity, stability, and resistance of the catalyst to carbon deposition. Research has demonstrated that strong metal–support interactions (SMSI) can enhance carbon-resistant performance by enhancing the dispersion and sintering resistance of active metals [51–55]. Therefore, the selection of an appropriate catalyst support must fully exploit its structural and physicochemical characteristics, such as its surface morphology, pore structure, thermal stability, redox properties, oxygen storage capacity, and surface basicity. Supports with a high porosity and surface area are ideal choices because they can provide a high reactivity and good dispersion of active metals while reducing the sintering of metal particles and promoting the reduction of metal precursors. Such choices can reduce or eliminate coke formation and enhance the interaction between the metal and support, thus improving the stability and carbon resistance of the catalyst.

In the DRM, commonly used supports include CeO_2, La_2O_3, TiO_2, ZrO_2, MgO, SiC, boron nitride (BN), Y_2O_3, TiO_2, Si_2O_3, Al_2O_3, activated carbon or charcoal, clay, and zeolite, as well as metal–organic frameworks (MOFs) [56]. The different supports exhibit different chemical properties. For example, CeO_2 exhibits a good oxygen storage capacity; La_2O_3, Y_2O_3, and TiO_2 provide a high oxygen mobility; ZrO_2 and BN offer excellent thermal stability; and SiC has a high thermal conductivity [57–63]. Consequently, both have the advantage of resisting carbon deposition. The following section discusses the effect of the supports on the catalyst’s resistance to carbon deposition. The catalytic performances of Ni-based catalysts supported on different supports are shown in Table 1 [64–75].

Table 1. Catalytic performance of a Ni-based catalyst supported on different supports.

Catalyst	Preparation Method	Reaction Conditions	Performance	Carbon Deposits (wt%)	Coke Formation Rate ($mgC/g_{cat.}/h$)	Main Type of Coke	Comments on Coke Formation	Ref.
6% Ni/Al_2O_3 nanofiber (F)	Incipient wetness impregnation	750 °C, 10 h, GHSV = 36 $L \cdot g^{-1} \cdot h^{-1}$	$X_{CO_2} \approx 81\%$ $X_{CH_4} \approx 83\%$	12	12	Graphitic carbon	Catalytic performance depended on alumina morphology.	[64]
6% Ni/Al_2O_3 nanosheet (S)	Incipient wetness impregnation	750 °C, 10 h, GHSV = 36 $L \cdot g^{-1} \cdot h^{-1}$	$X_{CO_2} \approx 83\%$ $X_{CH_4} \approx 85\%$	6	6	Graphitic carbon	Catalytic performance depended on alumina morphology.	[64]
10–20% Ni/Al_2O_3 (COMA)	One-pot	750 °C, 210 h, GHSV = 18 $L \cdot g^{-1} \cdot h^{-1}$	$X_{CO_2} = 96\%$ $X_{CH_4} = 99\%$ $H_2/CO = 0.89$	5	0.24	Graphitic carbon	Cage-like pore structure of COMA resisted coke growth by limiting available space around Ni.	[65]
Ni-SCS	Solution combustion synthesis	800 °C, 50 h, GHSV = 14.4 $L \cdot g^{-1} \cdot h^{-1}$	$X_{CO_2} = 98\%$ $X_{CH_4} = 95\%$ $H_2/CO = 0.90$	20.03	4	Filamentous carbon	Higher oxygen content and oxygen defect of the Ni-SCS catalyst led to surface carbon gasification.	[66]
Ni/BN-NC	Impregnation	750 °C, 100 h	$X_{CO_2} = 82\%$ $X_{CH_4} = 72\%$ $H_2/CO = 1.00$	Negligible	/	Graphitic carbon	Introducing BN support generated more oxygen vacancies. CeO_2 having oxygen vacancies increased carbon gasification rate.	[67]
Ni/MM-A	Incipient wetness impregnation	700 °C, 100 h, GHSV= 30 $L \cdot g^{-1} \cdot h^{-1}$	$X_{CO_2} = 85\%$ $X_{CH_4} = 75\%$ $H_2/CO = 0.76$	2.5	0.25	Carbon nanotubes	The fabricated macropores were beneficial to mass transfer and then to strong coke resistance.	[68]
$Ni/15\%CeO_2$-MgO	Co-precipitation	800 °C, 30 h, GHSV = 36 $L \cdot g^{-1} \cdot h^{-1}$	$X_{CO_2} = 95.2\%$ $X_{CH_4} = 93.7\%$ $H_2/CO = 1.03$	Negligible	/	MWCNTs	The occurrence of Ce^{3+} created charge imbalance, which led to the formation of oxygen vacancies through the transition from Ce^{3+} to Ce^{4+}, thereby increasing the amount of available oxygen.	[69]
$Ni/CeO_{0.38}Zr_{0.62}O_{2-\delta}$	Homogeneous deposition-precipitation	750 °C, 20 h	$X_{CO_2} = 60\%$ $X_{CH_4} = 50\%$ $H_2/CO = 0.5$~0.75	0.3	0.15	Graphitic and whisker carbon	Carbon formed from the CH_4 dissociation reacted with surface lattice oxygen of the catalyst support to form CO.	[70]
5%Ni/F-SBA-15	Ultrasonic impregnation	800 °C, 50 h, GHSV = 15 $L \cdot g^{-1} \cdot h^{-1}$	$X_{CO_2} = 85\%$ $X_{CH_4} = 86\%$ $H_2/CO = 1.27$	16.97	3.4	Amorphous carbon	The nickel fibrous SBA-15 catalysts showed moderate basicity, which boosted coke removal by reverse Boudouard reaction.	[71]

Table 1. *Cont.*

Catalyst	Preparation Method	Reaction Conditions	Performance	Carbon Deposits (wt%)	Coke Formation Rate (mgC/g_{cat}./h)	Main Type of Coke	Comments on Coke Formation	Ref.
5%Ni/DFSBA-15	Ultrasonic impregnation	800 °C, 50 h, GHSV = 15 $L \cdot g^{-1} \cdot h^{-1}$	X_{CO_2} = 87% X_{CH_4} = 88% H_2/CO = 0.84	8.08	1.6	Crystalline graphite	The nickel fibrous SBA-15 catalysts showed moderate basicity, which boosted coke removal by reverse Boudouard reaction.	[71]
$Ni_3Fe_1Cu_1$-MA	Co-precipitation	650 °C, 20 h, GHSV = 432 $L \cdot g^{-1} \cdot h^{-1}$	$X_{CH_4} \approx 15\%$ $H_2/CO \approx 0.5$	5	2.5	Graphitic carbon	Cu enhanced the interaction between Ni and Fe, inhibiting Fe segregation and reducing carbon deposition.	[72]
20Ni/ZnS-1	Incipient wet impregnation	750 °C, 12 h, GHSV = 51.4 $L \cdot g^{-1} \cdot h^{-1}$	X_{CO_2} = 75.4% X_{CH_4} = 84.5% H_2/CO = 1.87	38.3	31.9	Crystalline carbon	The stability of these catalysts was highly improved by reducing mass transfer constraints during DRM process.	[73]
Ni/fumed SiO_2	Pressure dilation	700 °C, 19 h, GHSV = 1440 $L \cdot gNi^{-1} \cdot h^{-1}$	X_{CH_4} = 92%	5.7	3	Carbon nanotubes	A significant increase in Ni dispersion resulted in a higher catalyst activity and increased stability.	[74]
Ni/ZSM-5	Microemulsion	750 °C, 80 h, GHSV = 30 $L \cdot g^{-1} \cdot h^{-1}$	X_{CO_2} = 62% X_{CH_4} = 53% H_2/CO = 0.80	12	1.5	Filamentous carbon	Catalytic activity was improved by homogenous distribution of surface acid–basic sites, thereby reducing the propensity of coke deposition.	[75]

3.1.1. Oxide-Supported Catalysts

CeO_2 has been successfully applied in thermal catalysis owing to its excellent oxygen storage capacity and redox properties generating mobile lattice oxygen and oxide vacancies [76,77]. Al-Fatesh et al. [78] reported an efficient CeO_2-based Ni-Ce/W-Zr catalyst, which utilized the redox shift of Ce to generate surface oxygen vacancies for in situ carbon suppression. As the concentration of Ce^{3+} increases, oxygen vacancies increase, accelerating the carbon gasification process to produce CO [78]. The lattice oxygen of CeO_2 has been found to oxidize carbon faster than the oxygen of CO_2 [79]. However, large Ni particles have a low metal–support interface, resulting in no contribution from the active metal surface to the carbon removal mechanism [80]. The introduction of dopants or their interactions with the CeO_2 support may enhance its performance. Akri et al. [30] synthesized atomically dispersed Ni on Ce-doped hydroxyapatite (HAP) catalysts using a strong electrostatic adsorption (SEA) method. Owing to the strong interaction between the Ni atoms and the HAP-Ce support, individual Ni atoms could only activate the initial C-H bond of CH_4, resulting in a negligible carbon deposition during the long-term DRM. The doping of Eu in CeO_2 increased the oxygen mobility and storage capacity, maintaining a balanced rate between the carbon formation and carbon oxidation, and resulting in a reduced accumulation of coke (Figure 4) [81]. CeO_2 doping can also attenuate the affinity between MgO and NiO_x through interactions with NiO, inhibit the formation of a NiO-MgO solid solution, and promote the reduction of Ni species [82].

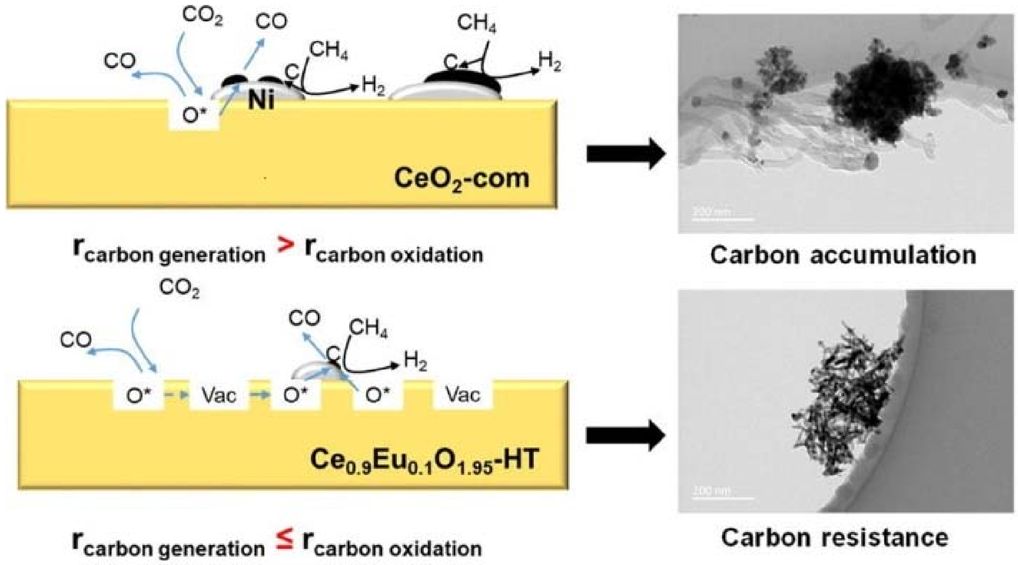

Figure 4. Catalytic mechanism for the reforming of methane by carbon dioxide and the percentage of CH_4-to-CO and CH_4-to-coke derived from CH_4 pulse experiments over Ni/CeO_2-com and Ni/$Ce_{0.9}Eu_{0.1}O_{1.95}$-HT [81]. O* is a reactive oxygen derived from CO_2. Copyright 2022, with permission from Elsevier.

La_2O_3, as a DRM support, can enhance the adsorption and activation of CO_2 [83]. Utilizing this characteristic, Zeng et al. [84] synthesized Ni_xGa_y/La_2O_3-MgO/Al_2O_3 layered double oxide (LDO), which enriched the CO_2 with La_2O_3 and continuously transferred it to Ga^{3+} for decomposition, generating sufficient active oxygen to eliminate carbon deposition (Figure 5). However, because of its low specific surface area, the dispersion of active metals on its surface is limited, and its resistance to carbon deposition and sintering needs to be improved. Song et al. [85] utilized KIT-6 as a template to synthesize mesoporous Ni-La_2O_3. This approach improves the adsorption and activation of CO_2 and enhances the effective dispersion of Ni. Consequently, it expands the interface between $La_2O_2CO_3$ and Ni, thereby facilitating the reaction between coke and $La_2O_2CO_3$ species and maintaining a cleaner and more active surface for Ni sites. The influence of preparation methods on carbon deposition morphology and its subsequent impact on the carbon resistance performance of Ni-La_2O_3 catalysts has been observed [57]. While the solvothermally synthesized Ni/La-SC catalyst produces amorphous carbon, other preparation methods such as solution combustion, sol-gel, homogeneous precipitation, and oleylamine-assisted methods result in filamentous carbon. This observation may offer insights applicable to catalysts employing unique carbon deposits as active sites or intermediates in reactions, albeit with consideration for the specific catalytic system and conditions.

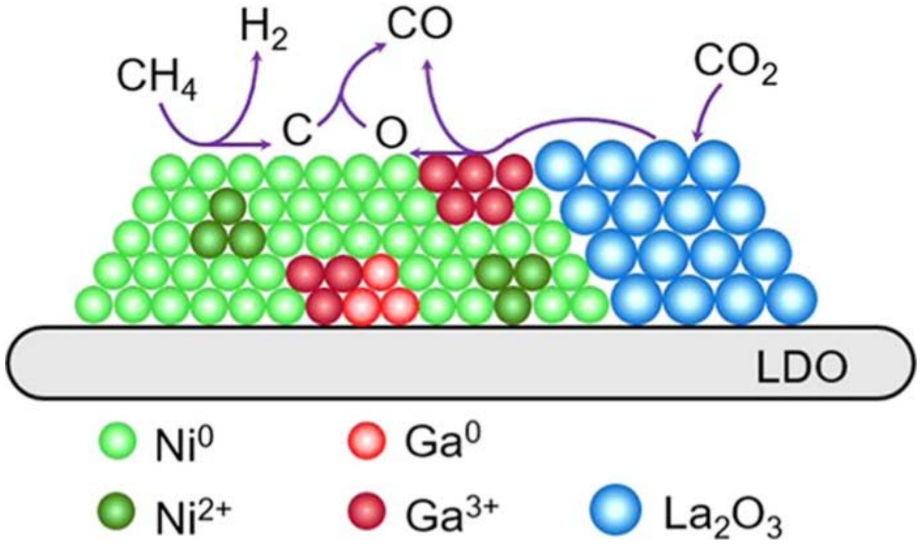

Figure 5. Reaction mechanisms for the DRM reaction catalyzed by the Ni/LDO, $Ni_{0.8}Ga_{0.2}$/LDO, and $Ni_{0.8}Ga_{0.2}/La_2O_3$-LDO catalysts [84]. Copyright 2021, with permission from the American Chemical Society.

Haug et al. [86] prepared a NiZr51 catalyst via a reaction between molten Ni and Zr foil. The catalyst consists of finely dispersed Ni nanoparticles that are relatively stable and resistant to sintering, and the Ni nanoparticles can undergo a process called anti-segregation, where carbon deposits segregate away from the active sites and migrate toward the ZrO_2 support. This anti-segregation process creates a carbophobic and oxophilic interfacial zone at the Ni/ZrO_2 interface, which protects the catalyst from coke formation. Then, they used a novel "reverse" chemical vapor deposition method to design a NiZr model catalyst, which is completely opposite to the preparation of traditional catalysts. This method involves depositing oxide islands on top of the active metal substrate to create a structurally "mirrored" system. This catalyst exhibits stable and high DRM activity, along with an enhanced resistance to coking [87]. The coke resistance of the catalysts strongly depended on the size of the Ni nanoparticles. Well-embedded and sufficiently small Ni nanoparticles (<10 nm) with a large metal-oxide phase boundary to ZrO_2 have short carbon diffusion pathways, allowing for the quick depletion of dissolved carbon.

However, large Ni domains are limited by relatively long carbon diffusion paths toward the phase boundaries, leading to a slower carbon clean-off and increased coking. The Ni-ZrO_2 with strong metal–support interactions prepared using ZrN (zirconium nitride) as a precursor of support was studied [88]. During calcination, the exchange of nitrogen and oxygen atoms induces structural transformations, creating strong interactions between Ni nanoparticles and the support. These interactions not only inhibit metal sintering but also promote CO_2 adsorption and activation by generating oxygen vacancies, aiding in carbon elimination. Wang et al. [89] indicated that the synergistic effect of oxygen vacancies and Ni species could promote the stability of Ni/ZrO_2 in the DRM at low temperatures. In DRM processes, the Ni species in the catalyst can undergo oxidation by CO_2 to form NiO species, and then be reduced back to Ni species by H_2 at 300 °C. This redox behavior helps to maintain the Ni species present on the catalyst surface, which are less prone to carbon deposition. The Ni/ZrO_2 catalysts benefit from the combined effect of Ni species and the oxygen vacancies on the catalyst surface. The Ni species promoted the activation of CO_2, whereas the oxygen vacancies aided in the removal of carbon species. This combined effect enhances the stability of the catalyst at low temperatures and prevents carbon deposition.

Owing to the strong metal–support interaction, a NiO-MgO binary catalytic system has been developed, but its resistance to carbon deposits and stability are unsatisfactory [90,91]. Recently, research has primarily focused on multi-support and spinel systems. Rosdin et al. [92] evaluated various oxide supports for the DRM reaction, including Al_2O_3, Al_2O_3-ZrO_2, and Al_2O_3-MgO, and the results indicated that Ni/Al_2O_3-MgO showed the best stability and activity as well as the least coke formation. Bagabas et al. [93] found that MgO content significantly affected the γ-Al_2O_3-supported Ni catalyst for the resistance to coke deposition. Zeng et al. [94] reported a mesoporous Ni/MgO-mSiO_2 catalyst; alkaline oxidized magnesium not only inhibits the sintering and deactivation of Ni at high temperatures but also promotes the cracking of CH_4 and the activation of CO_2 at the "Ni-MgO" interface formed in mSiO_2, thereby eliminating carbon deposition. Han et al. [95] developed a MgO-promoted Ni-CaO catalyst. Only 3.03 wt.% of coke after 30 h of the DRM and 0.0395 g of coke/g_{cat}. were generated after 10 DRM cycles. This can be attributed to the promotion of carbon removal from the surface by the NiO-MgO solid solution, resulting in the formation of fewer and softer carbon species on the surface [95]. The high surface area of $MgAl_2O_4$ spinel facilitates metal segregation. Sun et al. [96] have developed a $Mg_{1-x}Ni_xAl_2O_4$ catalyst with strong resistance to coke formation through a doping segregation strategy. The excellent resistance to coke formation is attributed to the smaller Ni particles and stronger metal–support interaction, which significantly inhibits the direct dissociation of CH_4 and promotes the oxidation of coke formation.

The structure of silica support on Ni-based catalysts can significantly affect the dispersion of active components [97]. Three silica supports, including silica spheres (MSS), MCM-41, and commercial silica, were investigated by Zhang et al. [97]. The presence of an inverted-tapered pore structure in the MSS facilitated the dispersion of the Ni active components in the constrained channels, resulting in the smallest Ni particle size and, thus, the minimum carbon produced during the reaction. Furthermore, the Ni/MSS prepared by the glycine-assisted and ethylene glycol-assisted impregnation reduced the Ni particle diameter, thereby inhibiting the formation of carbon deposits [98]. Song et al. [99] compared the effects of mesoporous and microporous silica on Ni nanoparticles. Benefitting from the confinement provided by the mesopores, the Ni nanoparticles were well embedded within the pores of Ni-SBA-15, exhibiting an excellent resistance to Ni sintering and carbon deposition. However, the microporosity of zeolite-β made it difficult to introduce Ni into the micropores, and the large Ni particles located outside the micropores reduced the overall performance. Ni-based catalysts with core–shell structures using silica and alumina as supports will be discussed later.

The catalytic activity of metal nanoparticles is influenced by their resistance to carbon deposition, which is significantly impacted by their size. Density functional theory (DFT) calculations on Ni nanoparticles of varying sizes on MgO(100) showed that the adsorption energy of the reaction intermediate CH_X depends on the Ni particle size [100]. Larger Ni particles exhibit a higher carbon growth energy and absolute carbon binding energy, leading to a preferential accumulation of carbon atoms on larger particles [100]. Zhang et al. [101] used a solid–solid phase transformation growth method to create porous single-crystal (PSC) MgO particles, which stabilize surface Ni nanocrystals and form an active metal oxide interface. The lattice structure and porosity of MgO reduces losses at grain boundaries during electron transfer, enhancing the DRM's catalytic performance and durability [101].

The morphology of the Al_2O_3 support significantly influences the resistance of the catalyst to carbon deposition. The flower-shaped Al_2O_3 nanostructure exhibits a sealing effect that leads to a less abundant population of active Ni sites on the carrier surface, resulting in a lower initial activity [102]. For spherical Ni/Al_2O_3, the weaker CO_2 activation capability and larger metal Ni particle size contribute to the substantial formation of filamentous carbon [102]. In contrast, filamentous Ni/Al_2O_3 demonstrates a higher resistance to coking, which was attributed to the surface dispersion of small Ni nanoparticles and strong SMSI [102].

3.1.2. Zeolite-Supported Catalysts

Zeolites are crystalline microporous aluminosilicate materials with high surface acidities that are widely used for C1 gas conversion [103,104]. However, zeolite acidity can hinder the adsorption of CO_2 onto zeolites. This is primarily due to the accumulation of dehydrogenated carbon deposits, which can lead to their polymerization of carbon deposits [33]. The basicity of zeolites can enhance the adsorption of acidic carbon dioxide molecules and suppress Boudouard reactions [105]. Therefore, several strategies have been applied to develop Ni zeolite catalysts, including the introduction of alkaline promoters and the use of high-silica or pure silica zeolites [75,106,107]. Zhu et al. [29] reported that the carbon deposition content of Ni@HZSM-5 catalyst after 50 h of reaction was below 0.43 wt%, which was attributed to the rigid structure of the zeolite and the combined effect of hydrogen spillage mediated by Ni in the zeolite, thereby inhibiting coke formation. Cheng et al. [108] have observed that within Ni-MFI, a fraction of Ni forms metal-oxygen ($Ni^{\delta+}$-$O^{(2-\xi)-}$) pairs with the zeolite framework, which follow the rapid transformation pathway of CH_X. Intermediate CH_X can be converted to CO and H_2 when exposed to CO_2, thereby effectively inhibiting carbon accumulation [108]. Moreover, the abundant SiO_x-$ONi^{\delta+}$ bonds control the oxidation state of Ni species during the DRM process, thereby limiting the deep dehydrogenation of CH_4 [109].

Silicalite-1 is commonly used to prevent the deactivation of metal species because of its ability to confine metal particles within its framework to form metal@zeolite catalysts [110]. One-pot Ni-anchored silicalite-1 showed superior resistance to carbon deposition compared to Ni/silicalite-1 prepared through the impregnation method in the DRM [107]. Encapsulation can control the size of Ni particles, and the complete encapsulation and strong metal–support interaction of Ni nanoparticles in Ni@silicalite-1 can sterically hinder the migration/aggregation deposition of carbon with a negligible coking content [111,112].

Liu et al. [113] developed Ni@silicalite-1 through a controlled “dissolution-recrystallization” method. During this process, Ni heteroatoms were incorporated into the zeolite lattice, forming Ni-O-Si bonds, which effectively stabilized the Ni nanoparticles and prevented their sintering or agglomeration. The embedded structure of the catalyst confines the Ni nanoparticles within the zeolite matrix, preventing their exposure to the reactants and reducing the chances of carbon deposition on the active sites. Additionally, the embedded structure facilitates the better access of oxygen to the carbon deposits, promoting their oxidation and minimizing coke accumulation. Controlling the coordination environment of Ni precursor complexes within the silicalite-1 allows for the optimization of the synergistic interaction between highly confined Ni nanoparticles (3–5 nm) in the zeolite micropores and the Lewis acid sites, thereby maintaining a beneficial balance between the formation and elimination of “in-process carbon” species [114]. Xu et al. [111] revealed that the Ni@SiO_2-S1 catalyst, synthesized using the seed-directed synthesis, exhibited a superior resistance to carbon deposition attributed to the complete encapsulation of Ni. Conversely, post-treatment and direct hydrothermal methods result in the incomplete encapsulation of Ni, leading to the formation of Ni phases on the external surface of the catalyst, rendering it more susceptible to deactivation. However, it should be noted that the synthesis of core–shell catalysts is relatively complex, and the presence of the shell can potentially result in reduced overall catalytic activity due to mass transfer limitations and the partial blocking of active metal sites. Nonetheless, researchers are dedicated to tackling the challenges associated with material synthesis and are exploring avenues such as refining synthesis techniques, optimizing shell design, and investigating thinner shell layers or novel shell materials to enhance the overall catalytic activity.

3.1.3. Other Supported Catalysts

Low thermal conductivity is a drawback of oxide-supported catalysts. This characteristic can result in uneven heat distribution, which is not ideal for the highly endothermic DRM. Silicon carbide (SiC) has excellent thermal conductivity [115]. SiC minimizes carbon deposition in the DRM [116]. Monolithic SiC-foam-supported Ni-La_2O_3 with a high thermal conductivity was developed, showing a more pronounced resistance to Ni sintering and carbon deposition than Ni-La_2O_3/Al_2O_3 [117]. The reaction atmosphere has a strong correlation with the catalyst stability. In an oxidizing atmosphere, the Ni species on the surface of the Ni/$MgAl_2O_4$ catalyst undergo oxidation and redispersion, while in a reducing atmosphere, the Ni species experience coking and sintering. Based on these findings, Feng et al. [118] proposed an alternating-feeding gas strategy to periodically change the gas flow direction, balance the structural evolution of Ni species within the catalyst bed, and enable the spontaneous regeneration of active sites, leading to a more stable DRM process.

The interface between the metal nanoparticles and BN suppressed coke formation. Zhang et al. [119] reported an interface-confined $NiMgAlO_x$/BN catalyst, showing an enhanced gas activation and inhibition of the deep cracking of CH_4 at the triple interface of Ni, BN, and $MgAlO_x$, resulting in an excellent resistance to coking. Zheng et al. [120] demonstrated that Mo doping could restrict the formation of filamentous carbon on Ni-halloysite nanotubes through steric hindrance effects and reduce the crystallinity of carbon deposition. The high melting point of Mo decelerates the sintering of the catalyst. Alli et al. [121] synthesized a MOF-derived Ni40%-Ce-BTC (benzene-1,3,5-tricarboxylate) catalyst by utilizing biphenyl-3,3′,5,5′-tetracarboxylic acid as the organic ligand. Owing to its smaller particle size, this catalyst exhibited a lower coke yield than the catalyst prepared by using terephthalic acid as the ligand.

3.2. Bimetallic and Alloying Ni-Based Catalysts

The surface chemical properties and morphological structures of catalysts are critical for DRM activity, selectivity, and coke formation. While single-metal catalysts excel in some areas, they have limitations that restrict their application. Therefore, the introduction of a second metal to form bimetallic or alloy catalysts has gained significant attention in recent years as a strategy for overcoming these limitations and improving catalytic performance through surface modification and control, alloy effects, and synergistic interactions [122].

This discussion focuses on two types of bimetallic catalysts: noble metal-nickel catalysts (Rh, Ru, and Pt) and early transition metal-nickel catalysts (Co, Fe, Cu, and Mo), whose catalytic performances of bimetallic and alloying catalysts are shown in Table 2 [27,75,98,123–140].

Table 2. Catalytic performances of bimetallic and alloying Ni-based catalysts.

Catalyst	Preparation Method	Reaction Conditions	Performance	Carbon Deposits (wt%)	Coke Formation Rate (mgC/gcat/h)	Main Type of Carbon	Comments on Coke Formation	Ref.
5Ni-Ta/FZSM-5	Microemulsion	750 °C, 80 h, GHSV = 30 $L\cdot g^{-1}\cdot h^{-1}$	X_{CO_2} = 97% X_{CH_4} = 91% H_2/CO = 0.97	5	0.65	Filamentous carbon	Catalytic activity was improved by homogenous distribution of surface acid–basic sites, thereby reducing the propensity of coke deposition.	[75]
5Ni5Co/SiO_2	Microemulsion anti-solvent extraction	750 °C, 25 h, GHSV = 24 $L\cdot g^{-1}\cdot h^{-1}$	X_{CO_2} = 88% X_{CH_4} = 91% H_2/CO = 0.9	Negligible	/	/	Ni/Co ratio determined carbon–oxygen balance eliminating coking.	[123]
10Ni0Co/SiO_2	Microemulsion anti-solvent extraction	750 °C, 25 h, GHSV = 24 $L\cdot g^{-1}\cdot h^{-1}$	/	7.2	2.88	Graphitic carbon	/	[123]
5Ni/MSS-EG	Ethylene glycol-assisted Impregnation	800 °C, 24 h, GHSV = 78 $L\cdot g^{-1}\cdot h^{-1}$	X_{CO_2} = 87.5% X_{CH_4} = 90.5% H_2/CO = 0.9	0.31	0.13	Graphitic carbon	Ethylene glycol-assisted impregnation minimized Ni particle size.	[98]
2.5% Ni-7.5% Co/KCC-1	Wet impregnation	700 °C, 8 h, GHSV = 36 $L\cdot g^{-1}\cdot h^{-1}$	X_{CO_2} = 92% X_{CH_4} = 85% H_2/CO = 0.9	14.5	18.1	graphitic carbon	The fibrous support restricted the deposition of coke.	[124]
3% Ni–9% Co/Mg(Al)O	Co-precipitation	600 °C, 25 h, GHSV = 120$L\cdot g^{-1}\cdot h^{-1}$	X_{CO_2} = 33% X_{CH_4} = 33% H_2/CO = 0.9	15.5	6.2	Graphitic carbon, carbon filaments	Alloying Ni with Co promoted the elimination of carbon species.	[125]
7.5Ni1Cu/Al_2O_3	Impregnation	700 °C, 7 h, GHSV = 14 $L\cdot g^{-1}\cdot h^{-1}$	X_{CO_2} = 70% X_{CH_4} = 64.5% H_2/CO = 0.85	3.5	5	Carbon nanofiber	A small amount of Cu promoted resistance to carbon deposits.	[126]
10NiO−MgO	Paper assisted combustion synthesis	700 °C, 26 h, GHSV = 14 $L\cdot g^{-1}\cdot h^{-1}$	X_{CO_2} = 95% X_{CH_4} = 82% H_2/CO = 0.85	3.9	1.5	Carbon nanotubes	Combustion synthesis prevented sintering and lead to the formation of a smaller crystallite size.	[127]
Ni/Al_2O_3-CeO_2-1.2% Gd_2O_3	One pot	800 °C, 6 h, GHSV = 27 $L\cdot g^{-1}\cdot h^{-1}$	X_{CO_2} = 94% X_{CH_4} = 86% H_2/CO =0.9	1.35	9.5	Filamentous carbon	Gd loading influenced the reducibility of Ni by weakening the formation of $NiAl_2O_4$.	[128]
$Ni_{0.8}$-$Co_{0.2}$/ZrO_2	Impregnation	700 °C, 80 h, GHSV = 275 $L\cdot g^{-1}\cdot h^{-1}$	X_{CO_2} = 93% X_{CH_4} = 92.8% H_2/CO = 0.78	5.00	/	/	The adsorbed oxygen remaining on Co oxidized the carbon deposits on Ni, restoring the metal surface.	[129]

Table 2. *Cont.*

Catalyst	Preparation Method	Reaction Conditions	Performance	Carbon Deposits (wt%)	Coke Formation Rate (mgC/gcat/h)	Main Type of Carbon	Comments on Coke Formation	Ref.
5% Ni-0.5% Ce/MCM-41	Capillary impregnation	800 °C, 100 h, GHSV = 21.6 $L \cdot g^{-1} \cdot h^{-1}$	X_{CO_2} = 78% X_{CH_4} = 70% H_2/CO = 0.93	3	0.3	Carbon nanotubes	The small amount of surface ceria provided oxygen species for the quick oxidation of carbon deposits.	[130]
$La(Co_{0.1}Ni_{0.9})_{0.5}Fe_{0.5}O_3$	Sol-gel self-combustion	750 °C, 30 h, GHSV = 12 $L \cdot g^{-1} \cdot h^{-1}$	X_{CO_2} = 80% X_{CH_4} = 70% $H_2/CO < 0.9$	0.08	0.026	Filamentous carbon	The synergistic effect between Ni and Co improved the anti-coking properties of the catalysts	[131]
$La(Co_{0.3}Ni_{0.7})_{0.5}Fe_{0.5}O_3$	Sol-gel self-combustion	750°C, 30 h, GHSV = 12 $L \cdot g^{-1} \cdot h^{-1}$	/	0.15	0.05	Filamentous carbon	/	[131]
Ni-Co-MOF/Al_2O_3	MOF synthesis	700 °C, 8 h, GHSV = 60 $L \cdot g^{-1} \cdot h^{-1}$	X_{CO_2} = 57% X_{CH_4} = 43% H_2/CO = 0.87	3.1	3.9	Amorphous carbon	The metal–organic framework showed low coke deposition at low temperatures.	[132]
7.5 wt% Ni-0.1Fe/$Ca_{12}Al_{14}O_{33}$	Impregnation	700 °C, 60 h	X_{CO_2} = 86% X_{CH_4} = 90.1% H_2/CO = 0.94	14.9	2.49	Filamentous carbon	Oxygen transferred by Fe/FeO redox enhanced the removal of carbon on the Ni surface.	[133]
Ni_4Fe_1/Mg (Al)O	Coprecipitation	700 °C, 25 h, GHSV = 60 $L \cdot g^{-1} \cdot h^{-1}$	X_{CO_2} = 86.8% X_{CH_4} = 79.5% H_2/CO = 0.85	0.7	0.28	Graphitic carbon	NiFe alloying inhibited CH_4 dissociation and promoted CO_2 activation, thus contributing to the suppression of coke deposition.	[134]
6Ni6Cu/MgAlO	Hydrothermal crystallization	700 °C, 70 h, GHSV = 40 $L \cdot g^{-1} \cdot h^{-1}$	X_{CO_2} = 87.2% X_{CH_4} = 85.2% H_2/CO = 0.96	2.7	0.386	Carbon nanotubes	The periclase phase provided abundant basic sites for the DRM and enhanced the metal–support interactions to promote the dispersion of nickel.	[135]
5 wt% Ni-15 wt% Cu/CeO_2	Co-impregnation	800 °C, 20 h, GHSV = 28.8 $L \cdot g^{-1} \cdot h^{-1}$	X_{CO_2} = 81% X_{CH_4} = 80% H_2/CO = 0.96	0.27	0.135	Filamentous carbon	The abundance of reactive oxygen species in Ni-O-Ce solid solution resulted in great coke resistance.	[136]
Ni-$Mo_{0.2}$/ZSM-5	Sequential impregnation	750 °C, 100 h, GHSV = 25 $L \cdot g^{-1} \cdot h^{-1}$	X_{CO_2} = 90% X_{CH_4} = 90% H_2/CO = 0.9	0.17	0.017	Graphitic carbon	Mo species anchored on zeolite contributed to the variation between MoO species and oxycarbide/carbide species, enabling dynamic carbon removal.	[137]

Table 2. *Cont.*

Catalyst	Preparation Method	Reaction Conditions	Performance	Carbon Deposits (wt%)	Coke Formation Rate (mgC/gcat/h)	Main Type of Carbon	Comments on Coke Formation	Ref.
$Ni_{3.49}$-Mo/MgO	Autothermal combustion	800 °C, GHSV = 60 $L{\cdot}g^{-1}{\cdot}h^{-1}$	X_{CO_2} = 100% X_{CH_4} = 100% H_2/CO = 1	Negligible	/	/	The locking mechanism of nickel nanoparticle growth was a crucial element in resisting coking and sintering.	[27]
3 wt% Ni-2 wt% In/SiO_2	Deposition-precipitation	675 °C, 24 h, GHSV = 40 $L{\cdot}g^{-1}{\cdot}h^{-1}$	X_{CO_2} = 70% X_{CH_4} = 30% H_2/CO = 0.77	Negligible	/	/	Ni-Ir dilution effect increased the dispersion of Ni on the catalyst surface and inhibited the formation of multi-bonded carbon species.	[138]
$Pt25Ni75/CeO_2$	Incipient wetness impregnation	650 °C, 24 h, GHSV = 72 $L{\cdot}g^{-1}{\cdot}h^{-1}$	X_{CO_2} = 52% X_{CH_4} = 50% H_2/CO = 0.7	0.013	0.54	Amorphous carbon	Metal–metal interactions and synergistic interactions improved the dispersion and reduction of metals and the reduction of cerium.	[139]
5 wt% Ru-1 wt% $Ni/MgAl_2O_4$	Wetness impregnation	750 °C, 6 h, GHSV = 60 $L{\cdot}g^{-1}{\cdot}h^{-1}$	X_{CO_2} = 96% X_{CH_4} = 93% H_2/CO = 0.96	0.7	1.17	Filamentous carbon	The addition of Ru reduced the metal Ni-support interaction dependent on the support.	[140]

3.2.1. Noble Metal-Nickel Catalysts

Rh-Ni Catalysts

The addition of Rh can alter the environment of Ni and significantly modify its electronic properties, enabling it to possess excellent anti-carbon deposition capabilities [141]. Mao et al. [142] found that adding Rh to Ni-$MgAl_2O_4$ can effectively balance the rates of CH_4 dissociation and CO_2 activation and prevent the further dissociation of CH_X* intermediates, thereby enhancing the coke resistance of the catalyst. Tang et al. [143] studied the reaction mechanisms of CH_4 dissociation on pure Ni and Rh-Ni catalysts using DFT calculations (Figure 6). On the pure Ni catalyst, the dissociation of CH_4 mainly follows $CH_4^* \rightarrow CH_3^* \rightarrow CH_2^* \rightarrow CH^* \rightarrow C^*$, while on Rh-Ni catalyst, the reaction path is $CH_4^* \rightarrow CH_3^* \rightarrow CH_2^* \rightarrow CH^* \rightarrow CHO^* \rightarrow CO^*$. This is because, with increasing Rh doping, the energy barrier for CHO* to CO* becomes significantly lower than that for CH* to C*, thereby preventing coke formation.

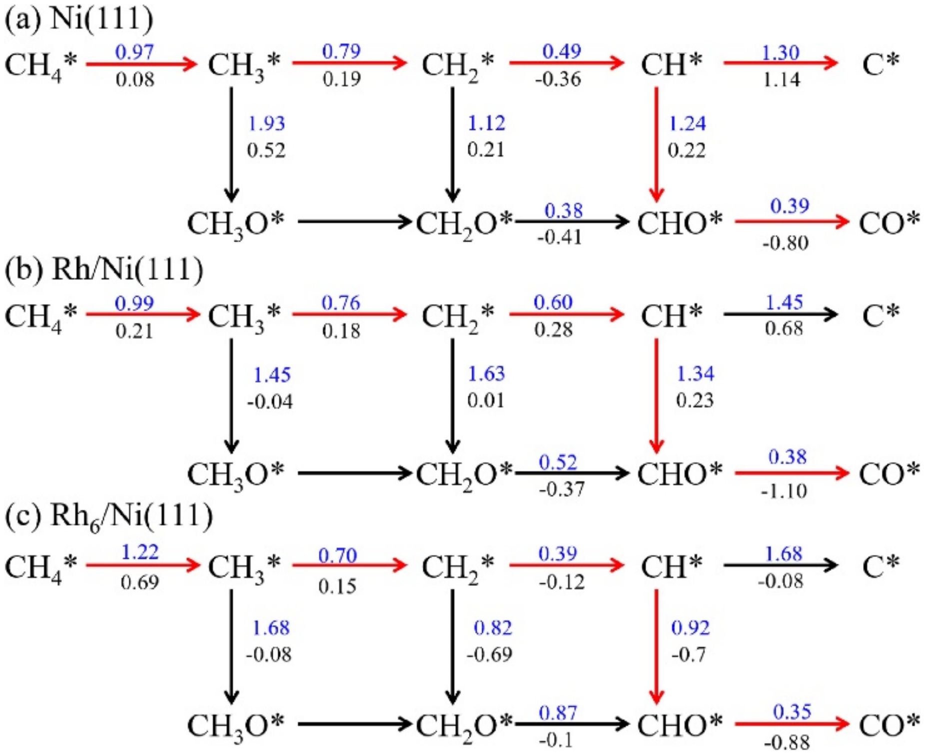

Figure 6. Reaction networks of CH_4 dissociation over Rh-Ni catalysts. The red arrow indicates the optimal reaction path. The blue number indicates the activation energy of the reaction, while the black number indicates the reaction energy, unit: eV [143]. * means the chemisorbed species. Copyright 2022, with permission from Elsevier.

Ru-Ni Catalysts

Through the study on the spent Ru-Ni-MgO catalyst, Zhou et al. [144] discovered that Ru could transform carbon deposits from the graphitic carbon type which is difficult to be gasified to a softer carbon type which can be easily gasified by CO_2. Furthermore, kinetic study reveals that Ru can mitigate the rate of carbon deposition by increasing the CH_4 activation barrier. An Operando DRIFTS study revealed that the presence of Ru atoms in the Ni-Ru/MgAl catalyst could hinder CO_2 conversion; nevertheless, it is beneficial for the gasification of carbonaceous adsorbates and prevents CO dissociation [145]. The presence of Ru in the Ni-Ru catalyst, with MFI zeolite as its support, also plays a role in accelerating the oxidation of carbon on the surface by CO_2 [146].

Pt-Ni Catalysts

Araiza et al. [139] reported that the Pt-Ni-CeO_2 catalyst demonstrated greater stability than the individual Pt and Ni catalysts. However, Pt-CeO_2 had the least amount of carbon deposition, suggesting that the stability of Pt-NiCeO_2 is not strongly related to carbon deposition. The mechanistic study demonstrated that the presence of Pt sites in Pt-Ni@CeO_2 was beneficial for the dissociation of CO_2 to generate surface oxygen. This surface oxygen can consume the surface carbon from CH_4 decomposition, thereby endowing the bimetallic Pt-Ni catalyst with a significantly improved resistance to coking. Niu et al. [147] prepared Pt-Ni catalysts supported on hydrotalcite. DFT calculations revealed that the energy barrier for CH* decomposition (CH* → C* + H*) was significantly increased on Pt-Ni catalysts compared to Ni catalysts. The energy barriers for the CH* + O* and carbon gasification (C* + O*) reactions on the Pt-Ni surface were also lower. Furthermore, the presence of Pt increased the surface oxygen density. These combined effects decrease the likelihood of surface coking on the catalyst.

3.2.2. Early Transition Metal-Nickel Catalysts

Co-Ni Catalysts

Because Co and Ni have similar electronic configurations, they can readily form bimetallic alloy nanoparticles [148]. Ni-Co alloying catalysts combine the high activity of Ni and excellent resistance with the carbon deposition of Co, making them highly promising catalysts for the DRM [149]. In the Boudouard reaction, the carbon formed on Co and NiCo is reactive and can be easily oxidized to CO. In contrast, carbon on Ni is less prone to oxidation, leading to deactivation during the DRM [150]. Co has a strong affinity for oxygen, which allows Ni-Co alloys to enhance the adsorption of CO_2 and suppress carbon deposition by promoting gasification [151,152].

The Ni/Co ratio adjusts the surface metal properties to produce highly active and durable DRM catalysts [153]. In the NiCo/$MgAl_2O_4$ catalysts, a Ni-to-Co ratio of 3:1 has shown optimal resistance to carbon deposition [154]. This improved performance can be attributed to the formation of enhanced alkaline sites and a higher number of surface metal sites with greater Ni-Co synergistic effects and selectivity for reactive coke deposition. Furthermore, Shakir et al. [155] synthesized a B-(Ni-Co)/$MgAl_2O_4$ with the assistance of $NaBH_4$ for the DRM. They demonstrated that a specific 3:1 ratio of Ni/Co, along with the synergistic effect of B and Co-doping, can lead to a higher metal dispersion and significantly reduce the carbon adsorption energy (E_{ads}) at various sites, thereby hindering surface carbon formation. However, Duan et al. [125] reported that Ni-Co/Mg(Al)O catalysts prepared using Mg-Al hydrotalcite-like compounds (HTlcs) as precursors with a Ni/Co ratio of 1:3 exhibited the best coke resistance. Similarly, Ni-Co/KCC-1 prepared by the sol-gel hydrothermal method showed the best anti-coking performance when the Ni/Co ratio was 1:3, which was also related to the fibrous nature of KCC-1, which restricted the sintering and aggregation of Ni particles [124]. Therefore, the optimal Ni/Co ratio depends on the specific catalyst formulation, precursor, and preparation method. Even slight changes in any parameter can significantly affect the synergistic effect of the NiCo alloy, the interactions between the metal carriers, and the formation and stability of active sites. Therefore, various factors need to be comprehensively considered to determine the optimal Ni/Co ratio. Moreover, the Co content affects the dispersion of Ni particles, and smaller Ni particles inhibit the formation and growth of carbon [156,157]. Chen et al. [158] studied the effects of the surface structure of NiCo alloys on the DRM using DFT calculations. Three NiCo alloy surface structures were constructed, as shown in Figure 7 [158]. The carbon removal was the rate-controlling step on the Ni surface of NiCo(121). Therefore, a high coverage of C* can potentially lead to catalyst deactivation owing to carbon accumulation. On the Co surface of NiCo(121), the dissociation of methane is the sole rate-controlling step, while the dissociation of CO_2 reaches equilibrium, resulting in a low C deposition and high O deposition. In contrast, the coverage of C*and O*on the NiCo(211) surface is moderate, leading to a stable catalyst performance. Microkinetic studies show that during the activation stage of the Ni-Co alloy, Ni and Co atoms are segregated, with Ni atoms migrating toward the outer surface of the alloy and Co atoms migrating toward the center, as shown in Figure 8 [40]. Furthermore, the average C and O adsorption energies were influenced by the Ni/Co ratio. This means that the relative contents of Ni and Co in the alloy affect the adsorption behavior of C and O atoms on the surface of the alloy; therefore, by adjusting the Ni/Co ratio, the surface carbon and oxygen contents can be balanced, thereby optimizing catalytic performance. $Ni_{0.2}Co_{0.3}$/silicalite-2 exhibits optimal activity and shows no carbon deposition. DFT calculations revealed that the segregation of Co could facilitate a charge transfer from the surface to CO_2 [159]. Within a certain range, a higher concentration of Co on the Ni surface led to an increased charge of the CO_2 adsorbed, thereby enhancing the activation capability of CO_2. This results in the generation of more O and OH species that participate in the oxidation of CH and the hydrogenation of carbon.

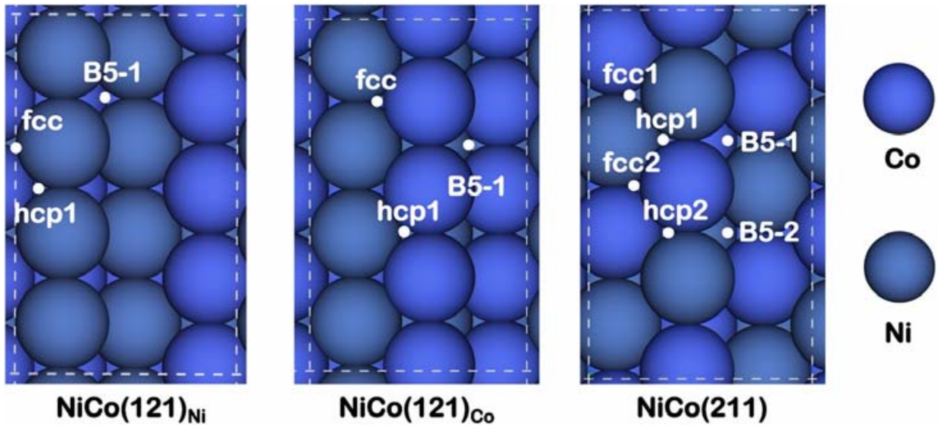

Figure 7. Surface structure of NiCo(121)Ni, NiCo(121)Co, and NiCo(211). The different surface sites are also marked [158]. Copyright 2022, with permission from Elsevier.

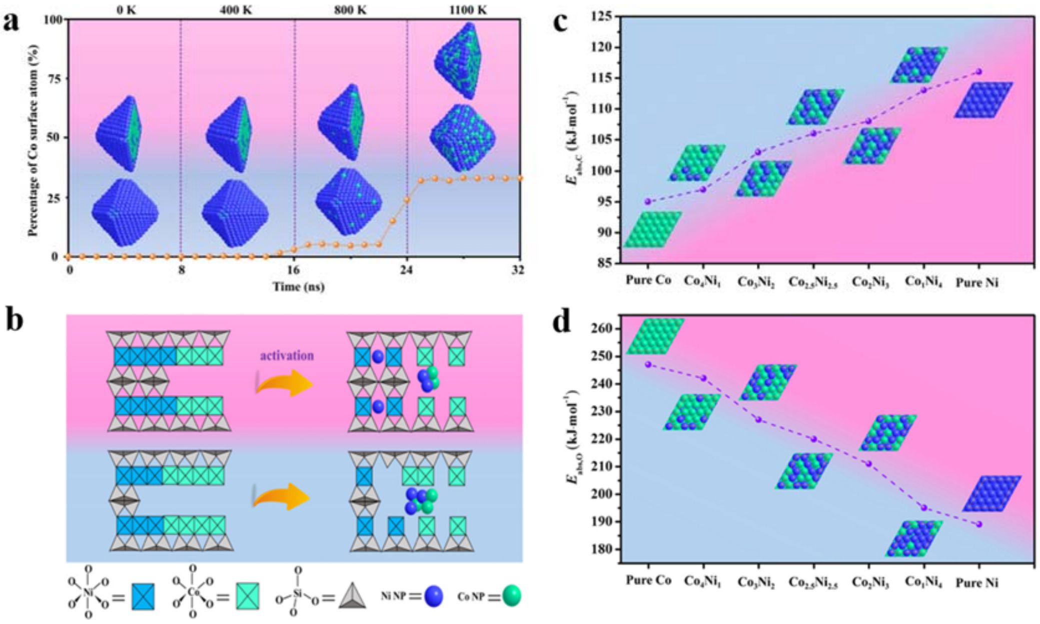

Figure 8. (**a**) Temperature dependence of the relative percentage of surface Ni atoms in a Co core–Ni shell NP. Cyan and blue spheres correspond to Co and Ni atoms, respectively. (**b**) Evolution of metal NPs for phyllosilicates. (**c**,**d**) C and O adsorption energies calculated on Co(111), NiCo(111), and Ni(111) surfaces [40]. Copyright 2022, with permission from the American Chemical Society.

Liu et al. [160] have indicated that the doping of Co could serve as an effective CO_2 adsorption site and potentially enhance CO_2 activation, thereby providing more oxygen atoms for the easy consumption of coke. Li et al. [161] synthesized a highly carbon-resistant Ni-Co catalyst supported on bimodal mesoporous alumina. The high carbon resistance of the material is attributed to the enhanced mass transfer provided by its sizeable mesoporous structure, as well as the Ni-Co alloy which increased the activation energy of the CH_4 consumption with an excellent suppression of CH_4 dissociation [161].

The synthesis strategy has a significant impact on the anti-coking properties of the catalysts. For instance, Ni-Co/SiO_2 prepared by the ammonia reflux impregnation method utilizes ammonia to reduce the acidity of the support, thereby increasing the adsorption of CO_2 and promoting the carbon removal reaction [162]. Micro-emulsion coupling with an anti-solvent extraction strategy can form droplets encapsulating the precursor of the Ni-Co/SiO_2, thereby leading to a narrow distribution of particle sizes and enhancing the adjacent distribution of Ni and Co [123]. This enables a more optimized balancing of C* and O* on the Co-Ni alloy, potentially eliminating coking. Moreover, the anchoring of Ni-Co alloys onto defective h-BN nanosheets significantly enhances the carbon removal rate, resulting from defective h-BN, with its favorable basicity, improving the adsorption of CO_2 on the catalyst surface, thereby facilitating the elimination of inert carbon species [163]. Small amounts of Ce and Mg-doping agents can adjust the acidity/alkalinity of the support [164]. The Ni-Co alloy catalysts supported on Ce and Mg co-modified Al_2O_3 showed improved CO_2 adsorption and a higher oxygen storage capacity owing to the modification of Al_2O_3. After 500 h of reaction, only 2.40 mmol/g of carbon was deposited [164].

Fe-Ni Catalysts

Because of the cost-effectiveness of Fe and its excellent redox performance, it is suitable for forming alloys with Ni to create coke-resistant bimetallic catalysts [165,166]. Kim et al. [167] elucidated the promoting role of Fe in bimetallic Ni-Fe catalysts, which underwent partial oxidation to form FeO that migrated to the surface. It then underwent Fe^{2+} O/Fe redox cycling with carbonaceous deposits, resulting in the generation of CO. The peak of Ni^0 remains unchanged after a 2 h DRM reaction; the ratio of Ni^0 to Ni^{2+} is 0.19, and the ratio of Fe^0 to Fe^{n+} (n = 2 and 3) decreases from 0.79 to 0.21, indicating that the oxidation cycle of Fe effectively inhibits the oxidation of Ni^0 [168].

Different Ni/Fe ratios affected the catalytic performance. The Fe-Ni/$MgAl_2O_4$ with a Fe/Ni ratio of 0.7 exhibits a high selectivity toward CO and has a CO/H_2 ratio close to 1, following the Mars-van Krevelen mechanism [166]. The 3–4 nm Ni-Fe nanoparticles, with a Ni/Fe ratio of 3, displayed enhanced stability for DRM reactions. However, at high reaction temperatures (850 °C), a structural transformation from Ni^0/FeO to Ni–Fe/FeO can occur [169]. However, Fe^0 segregation was ineffective in facilitating coke removal. To solve this dealloying process, Li et al. [170] designed Ni1Fe/Al (O) with an equimolar amount of Ni and Fe using an evaporation-induced self-assembly approach. The Ni1Fe1 alloy gradually evolved into a stable Ni_3Fe_1 alloy owing to the iron-surplus strategy, and the segregated Fe, in turn, formed FeO_x, which played a role in carbon gasification, thereby reducing the amount of coke deposition and the degree of graphitization. Huang et al. [171] indicated that the presence of Fe increased the lattice oxygen content of the Ni-Fe/MC12A7, resulting in the formation of a small amount of H_2O through the reaction with CH_4. The dissociation of H_2O can decrease the surface coverage of C* ($C^* + H^* \rightarrow CH^*, C^* + OH^* \rightarrow CO^* + H^*$) and consume C_α on the catalyst [171]. The kinetic study of the Fe-promoted Ni-MgO catalyst reveals that the surface oxygen coverage is determined by the Fe/Ni ratio and the contact atmosphere (CO_2 concentration), which influences the rate of coke deposition and the gasification rate without changing the kinetics and mechanism of the Ni catalyst (Figure 9) [172].

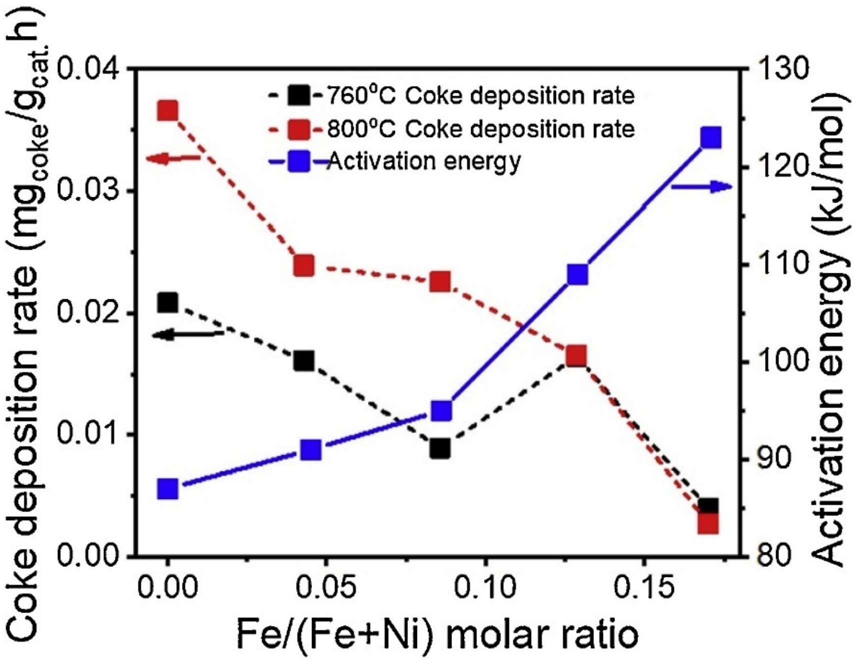

Figure 9. Coke deposition rates and activation energies of $Fe_xNi_yMg_{1-x-y}O$-R catalysts as a function of Fe/(Ni + Fe) molar ratios [172]. Copyright 2020, with permission from Elsevier.

Mo-Ni Catalysts

Although molybdenum is not active in dry reforming reactions, the addition of Mo can form alloys with Ni, thereby improving the catalytic conversion and oxidation resistance of CH_4/CO_2 reforming [173].

Song et al. [27] reported a Mo-doped Ni nanocatalyst supported on defect-free single-crystal MgO. Notably, no coking was detected even after 850 h of the DRM. This exceptional performance can be attributed to the activation process, where the Ni particles migrated toward the high-energy step edges of crystalline MgO(111), forming stable and persistent nanoparticles with an average size of 17 nm. The migration and stabilization of Ni nanoparticles on MgO(111) is crucial for achieving remarkable anti-coking and anti-sintering activities. The opposite result has also been reported: severe coking occurs when defect-rich MgO is used as a catalyst support [27,174]. Certain studies indicate that the presence of Mo can decrease the catalytic activity of Ni/Al_2O_3 in the DRM because the formation of the $MoNi_4$ phase in $Ni\text{-}Mo/Al_2O_3$ leads to a reduced interaction between NiO species and Al_2O_3, resulting in a decrease in both their mutual reactivity and basicity [175]. Abdel Karim Aramouni et al. [176] indicated that the nitriding treatment of $Ni\text{-}Mo/MgO\text{-}Al_2O_3$ can effectively reduce the formation of carbon whiskers, which is related to the preferential adsorption of CH_4 by Ni-Mo nitrides.

Zhang et al. [137] developed a Ni-Mo alloy catalyst anchored on ZSM-5 and elucidated its distinct reaction mechanism compared with that of Ni/ZSM-5. For Ni/ZSM-5, the primary reaction intermediate is the carbonate species, which competes with the CH_x species, leading to direct CH_x decomposition and carbon formation (Figure 10). However, for Ni-Mo/ZSM-5, the primary reaction intermediate was the formate species, which readily reacted with hydrogen species to form products. Additionally, the Mo species in Ni-Mo/ZSM-5 underwent a cycle from MoO_x to MoO_xC_y, which effectively prevented carbon formation and enhanced the stability of the catalyst.

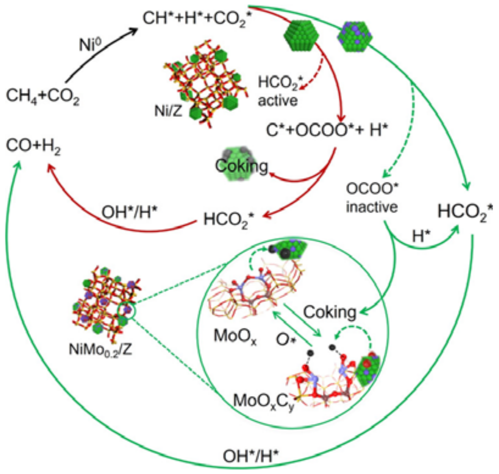

Figure 10. Proposed catalytic reaction pathways for the DRM over Ni/Z and NiMo$_{0.2}$/Z catalysts. The green line represents the reaction pathway of NiMo$_{0.2}$/Z, and the red line represents the reaction pathway of Ni/Z. The dashed arrow indicates the minor products during the DRM reaction. The solid arrow represents the major reaction pathway. Ni: green, Mo: purple, O: red, and C: black [137]. * means the surface species. Copyright 2021, with permission from the American Chemical Society.

Tang et al. [177] discovered that Mo doping could enhance the strength of alkaline sites in Ni-HAP (hydroxyapatite), and the synergistic effect of hydroxyl groups with the Ni-Mo alloy played a role in the oxidation of carbon deposits and the partial oxidation of methane at the initial reaction time. Wang et al. [178] analyzed the surface coverage of various intermediate species on Ni(111)MoO$_x$, as shown in Figure 11. On the Ni(111) surface, C* (adsorbed carbon) is the primary surface species, and its coverage increases with temperature. Nevertheless, after Mo doping, O* (oxygen adsorbed on the site not directly affected by the doped Mo atom) or O$^{\#}$ (oxygen adsorbed on the site affected by the doped Mo atom) becomes dominant, and can eliminate C*, thereby enhancing the resistance to carbon deposition.

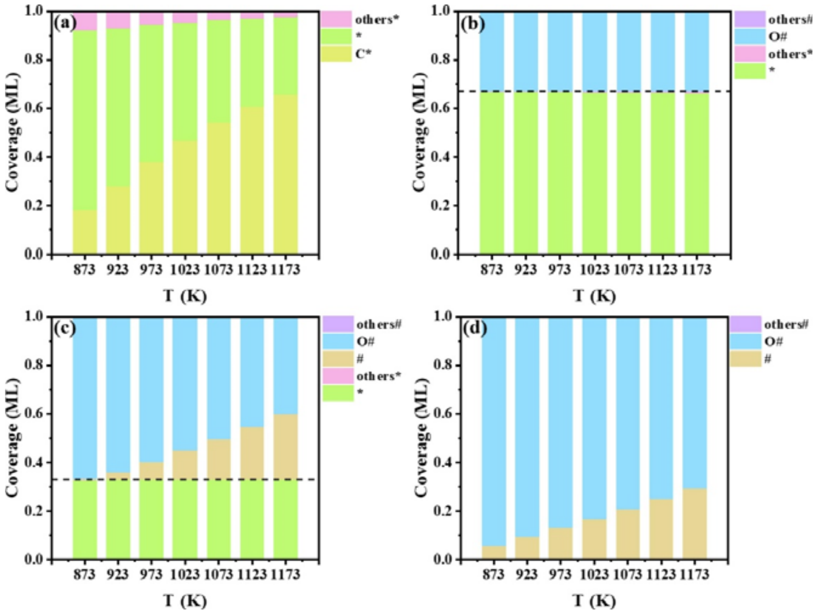

Figure 11. Variation of the surface coverage of the main intermediate species on the Ni(111) (**a**), NiMo$_1$(111) (**b**), NiMo$_2$(111) (**c**), and NiMo$_3$(111) (**d**) in the temperature range of 873.15–1173.15 K [178]. * means the site not directly affected by the doped Mo atom and $^{\#}$ means the site affected by the doped Mo atom. Copyright 2022, with permission from Elsevier.

Cu-Ni Catalysts

Because of the similarity in the lattice constants of Cu and Ni, Ni-Cu bimetallic catalysts have recently been utilized to develop catalysts with a high resistance to coking and enhanced DRM activity [126,135,179–183].

Song et al. [179] indicated that the Ni-Cu composition significantly affects the activity and stability of the Ni-Cu/Mg(Al)O catalyst. When the Cu concentration was low, the surface-segregated Cu atoms preferentially occupied the flat terrace positions of Ni without the ability to suppress carbon deposition. However, at high Cu concentrations, the formation of Cu clusters promotes carbon formation. Han et al. [180] demonstrated that 5 nm Cu-Ni alloy nanoparticles with a Cu/Ni ratio of 1/8 exhibited an optimal resistance to coking. This is because a moderate amount of Cu enhances the conversion of the CH_x species on Ni to syngas, thereby avoiding the deep cracking of the CH_x species.

Similarly, Chatla et al. [181] reported that Cu-Ni/Al_2O_3 with a Cu/Ni ratio of 1/8 exhibited optimal activity and stability. This is attributed to its ability to generate more amorphous carbon with lower graphitic carbon content. DFT simulations demonstrated that the addition of an appropriate amount of Cu increased the activation energy barrier for CH_x dehydrogenation and significantly reduced the activation energy barrier for carbon elimination via gasification. Xiao et al. [135] designed Ni-Cu alloy nanoparticles anchored on $MgAlO_x$ nanosheets, which were highly dispersed to improve the metal–support interactions and prevent the aggregation and sintering of the metal particles. Additionally, the presence of Cu atoms on the Ni(111) surface balanced the adsorption of C* and O* species, suppressing carbon accumulation and coke formation.

3.3. Structured Approaches for Anti-Carbon Catalysts

Structured approaches for anti-carbon catalysts in the DRM process involve designing and developing catalysts with specific structures and compositions to enhance the resistance against coke formation and prolong catalyst activity during the DRM. The performances of Ni-based catalysts with different structures are presented in Table 3 [111,135,184–201].

3.3.1. Core–Shell Catalysts

The synthesis strategy of core–shell structured catalysts is extensively utilized for high-temperature chemical reactions with the aim of enhancing their resistance to sintering and carbon deposition [202–205]. These core–shell catalysts exhibit a superior thermal stability and resistance to sintering, resulting in reduced coke formation and deactivation rates during DRM reactions compared with traditional catalysts [116,184,193,206].

The Ni@SiO_2 catalyst is one of the most extensively studied catalysts in this field. The confinement effect of the SiO_2 shell restricts the movement of Ni nanoparticles, preventing their aggregation and maintaining an average size of approximately 5 nm [184]. Kaviani et al. [194] successfully synthesized a core–shell structured Ni-SiO_2 catalyst, leveraging the protective SiO_2 shell to prevent Ni sintering and suppress carbon formation. However, carbon deposition tended to increase at high Ni loadings (e.g., 15 wt.%). This can be attributed to weaker metal–support interactions, which limit the ability of SiO_2 to effectively hinder the migration of Ni particles, consequently leading to a reduced metal dispersion and larger particles. Small Ni particles are beneficial for minimizing carbon deposition. The In-Ni alloy nano-catalysts ($In_xNi@SiO_2$) with a silica shell confinement with remarkable coking resistance over a period of 450 h [197]. The electron transfer between the In and Ni alloys, coupled with the presence of a silica shell, significantly reduces the rate of carbon deposition and enhances the overall coking resistance by limiting the migration and aggregation of the alloy particles. Introducing Co with oxygen-affinity properties into Ni@SiO_2 helps minimize the aggregation of Ni-Co nanoparticles. It also activates CH_4 and CO_2 molecules, making them more reactive and less likely to form coke precursors [207].

Table 3. Catalytic performance for structured Ni-based catalysts.

Catalyst	Preparation Method	Reaction Conditions	Performance	Carbon Deposits	Coke Formation Rate (mgC/gcat/h)	Main Type of CARBON	Reason for Coke Resistance	Ref.
Ni@SiO_2 (core–shell)	Microemulsion	650–800 °C, 50 h, GHSV = 18 $L{\cdot}g^{-1}{\cdot}h^{-1}$	X_{CO_2} = 71–90% X_{CH_4} = 63–85% H_2/CO = 1	0.7	0.14	Amorphous carbon	High coke resistance attributed to small Ni particle size and confinement effect of shell.	[184]
NiCo@SiO_2 (core–shell)	Microemulsion	800 °C, 1000 h, GHSV = 300 $L{\cdot}g^{-1}{\cdot}h^{-1}$	X_{CO_2} = 88.9 X_{CH_4} = 87.2 H_2/CO = 1	Negligible	/	/	NiCo alloy core–shell showed higher activity and selectivity than monometallic catalysts.	[185]
RuCo@SiO_2 (core–shell)	Hydrothermal and modified Stöber	700 °C, 10 h, GHSV = 54 $L{\cdot}g^{-1}{\cdot}h^{-1}$	X_{CO_2} = 84.7 X_{CH_4} = 74.4 H_2/CO = 0.98	0.5	0.5	Amorphous carbon	Surface distribution of Ru and shell porosity were important factors in the DRM performance.	[186]
Ni-ZrO_2@SiO_2 (core–shell)	One-pot and microemulsion	800 °C, 240 h, GHSV = 18 $L{\cdot}g^{-1}{\cdot}h^{-1}$	X_{CO_2} = 93.2 X_{CH_4} = 90.5 H_2/CO = 0.95	Negligible	/	/	ZrO_2 promoted reducibility of NiO, available oxygen species and increased Ni dispersion.	[187]
Ni@HSS (yolk–shell)	One-pot microemulsion	800 °C, 55 h, GHSV = 144 $L{\cdot}g^{-1}{\cdot}h^{-1}$	X_{CO_2} = 95 X_{CH_4} = 94.5 H_2/CO = 0.93	Negligible	/	/	Facile synthesis method for multiple small Ni nanoparticles anchored strongly inside silica hollow sphere.	[188]
Ni@NiPhy @SiO_2 (core–shell)	Hydrothermal and Stöber	700 °C, 600 h, GHSV = 36 $L{\cdot}g^{-1}{\cdot}h^{-1}$	X_{CO_2} = 95 X_{CH_4} = 94.5 H_2/CO = 0.8	5.5	0.09	Carbon nanotubes	Confinement effect improved metal–support interaction and prevented carbon nanotube growth.	[189]
Ni/$MgAl_2O_4$ @SiO_2 (core–shell)	Sol-gel coating	750 °C, 10 h, GHSV = 12 $L{\cdot}g^{-1}{\cdot}h^{-1}$	X_{CO_2} = 80 X_{CH_4} = 70 H_2/CO = 1	Negligible	/	/	Ni/$MgAl_2O_4$ prepared using solution-combustion were coated with silica, showing good coating and coke resistance.	[190]
@SiO_2@Ni @ZrO_2 (sandwich)	Sol-gel coating	700 °C, 20 h, GHSV = 24 $L{\cdot}g^{-1}{\cdot}h^{-1}$	X_{CO_2} = 60 X_{CH_4} = 60 H_2/CO = 0.75	Negligible	/	/	Higher binding energy of CO_2 caused CO_2 enrichment on surface and lowered coke formation.	[191]
Al_2O_3@Ni @Al_2O_3 (sandwich)	Atomic layer deposition	800 °C, 70 h, GHSV = 300 $L{\cdot}g^{-1}{\cdot}h^{-1}$	X_{CO_2} = 95 X_{CH_4} = 92 H_2/CO = 0.75	Negligible	/	/	Double interaction between Ni and γ-alumina support and alumina coating increased resistance to sintering and deactivation.	[192]

Table 3. *Cont.*

Catalyst	Preparation Method	Reaction Conditions	Performance	Carbon Deposits	Coke Formation Rate (mgC/gcat/h)	Main Type of CARBON	Reason for Coke Resistance	Ref.
Ni-SiO_2@CeO_2 (core–shell)	Ammonia evaporation	600 °C, 72 h, GHSV = 200 $L{\cdot}g^{-1}{\cdot}h^{-1}$	$X_{CO_2} = 94$ $X_{CH_4} = 92$ $H_2/CO = 0.5$	Negligible	/	/	The confinement effect of the ceria shell on the Ni nanoparticles and strong redox ability of ceria contributed to the coke inhibition properties of Ni-SiO_2@CeO_2.	[193]
Ni-SiO_2@SiO_2 (core–shell)	Ammonia evaporation	700 °C, 12 h, GHSV = 18 $L{\cdot}g^{-1}{\cdot}h^{-1}$	$X_{CO_2} = 93$ $X_{CH_4} = 72.5$ $H_2/CO = 0.95$	Negligible	/	/	The encapsulation structure of the Ni-SiO_2@CeO_2 catalyst provided strong metal–support interaction that led to anti-sintering and low coke formation.	[194]
Ni@SiO_2 (yolk–shell)	Reverse microemulsion	700 °C, 30 h, GHSV = 48 $L{\cdot}g^{-1}{\cdot}h^{-1}$	$X_{CO_2} = 80$ $X_{CH_4} = 72.5$ $H_2/CO = 0.9$	Negligible	/	/	The yolk–shell nanoreactors had excellent resistance to metal sintering and coke formation.	[195]
$Pt_{0.25}$-NiCe @SiO_2 (yolk–shell)	Reverse microemulsion + wetness impregnation	500 °C, 20 h, GHSV = 60 $L{\cdot}g^{-1}{\cdot}h^{-1}$	$X_{CO_2} = 6\%$ $X_{CH_4} = 10\%$ $H_2/CO = 0.49$	3.5	1.75	Filamentous and graphitic carbon	A synergetic combination of the confined yolk–shell morphology and Pt-Ni SAA structures prevented carbon formation and provided excellent catalyst stability.	[196]
$In_{0.5}Ni$@SiO_2 (core–shell)	One-pot micelle	800 °C, 430 h, GHSV = 18 $L{\cdot}g^{-1}{\cdot}h^{-1}$	$X_{CO_2} = 96\%$ $X_{CH_4} = 95\%$ $H_2/CO = 1.0$	5%	0.12	Amorphous and graphitic carbon	$In_{0.5}Ni$@SiO_2 bimetallic catalysts exhibited excellent carbon resistance owing to the electronic, structural, and confinement effects of indium.	[197]
6Ni6Cu/M @gAlO (sandwich)	Hydrothermal crystallization	700 °C, 70 h, GHSV = 40 $L{\cdot}g^{-1}{\cdot}h^{-1}$	$X_{CO_2} = 87.2\%$ $X_{CH_4} = 85.2\%$ $H_2/CO = 0.96$	0.27	0.039	Carbon nanotubes	The periclase phase provided abundant basic sites and enhanced the metal–support interactions to promote the dispersion of Ni.	[135]
2Ni@1Mo-HSS (yolk–shell)	One-pot microemulsion	800 °C, 72 h, GHSV = 240 $L{\cdot}g^{-1}{\cdot}h^{-1}$	$X_{CO_2} = 92\%$ $X_{CH_4} = 92\%$ $H_2/CO = 0.91$	Negligible	/	/	The formation of SiMoO species promoted an increase in the number of acidic sites on the support, which helped activate methane.	[198]

Table 3. *Cont.*

Catalyst	Preparation Method	Reaction Conditions	Performance	Carbon Deposits	Coke Formation Rate (mgC/gcat/h)	Main Type of CARBON	Reason for Coke Resistance	Ref.
Ni-CeO_2@SiO_2 (core–shell)	One-pot	750 °C, 50 h, GHSV = 60 $L \cdot g^{-1} \cdot h^{-1}$	X_{CO_2} = 82 X_{CH_4} = 80 H_2/CO = 0.88	0.1	0.02	Graphitic carbon	The SMSI promoted the ceria surface lattice oxygen mobility and generated more oxygen vacancies, reducing carbon deposition.	[199]
Ni@S-1 (core–shell)	Microemulsion and crystallization	700 °C, 70 h, GHSV = 240 $L \cdot g^{-1} \cdot h^{-1}$	X_{CO_2} = 75 X_{CH_4} = 75 H_2/CO = 0.95	0.9	0.13	Graphitic carbon	The core–shell structure with active metal nanoparticles encapsulated by the support shell prevented sintering and coke formation.	[200]
Ni@SiO_2-S1 (core–shell)	Seed-directed synthesis	700 °C, 28 h, GHSV = 750 $L \cdot g^{-1} \cdot h^{-1}$	X_{CO_2} = 80 X_{CH_4} = 73 H_2/CO = 0.9	0.5	0.18	Graphitic carbon	The full encapsulation of Ni in the support with small Ni particle sizes and strong metal–support interactions protected Ni aggregation and inhibited coke formation.	[111]
Ni/Kaol (sandwich)	Wet impregnation	750 °C, 100 h, GHSV = 6 $L \cdot g^{-1} \cdot h^{-1}$	X_{CO_2} = 60 X_{CH_4} = 58 H_2/CO = 0.86	5.9	0.59	Graphitic carbon	Owing to the confinement and isolation effects of the kaolinite nanosheets, the Ni-Kaol catalyst maintained a high catalytic stability.	[201]

Core–shell catalysts composed of different materials for the shell and core have also received significant attention. Ni-ZrO_2@SiO_2 catalysts with multiple Ni-ZrO_2 cores and mesoporous silica shells exhibit an excellent resistance to coking and sintering in DRM reactions at 800 °C [187]. The microporous SiO_2 shell effectively encapsulates the Ni-ZrO_2 nanoparticles, preventing the aggregation of Ni on the outer surface of the silica spheres. This encapsulation enhances the interaction between NiO and ZrO_2, leading to an improved reducibility of NiO and an increase in active sites. Lin et al. [208] found that the Ni-CeO_2@SiO_2 catalyst prepared using a one-pot method was superior to that prepared using an impregnation method. After a 100 h durability test at 800 °C, no carbon deposition was detected, but the size of the Ni particles increased. The CeO_2 shell also enhances the H_2S tolerance of the NiCo-MgAl@CeO_2 catalyst [209]. Cobalt can modify the chemical adsorption kinetics of sulfur, while the lattice oxygen of the CeO_2 shell oxidizes and removes H_2S through continuous replenishment of CO_2. The Ni-Cu alloy encapsulated by silica nanospheres has difficulty in fully gasifying the carbon precursor CH_x on the alloy surface without the assistance of lattice oxygen from the carrier, resulting in the deposition of trace amounts of carbon (0.3 wt.%) [210]. In (Ni-Cu/CeO_2)@SiO_2 with CeO_2 as the support and SiO_2 as the shell, the metal–support interaction effect of Ni-Cu and CeO_2 enhances the surface lattice oxygen migration rate of cerium dioxide, resulting in more oxygen vacancies, allowing for the almost complete gasification of deposited carbon [199]. Additionally, the physical confinement of SiO_2 nanoparticles prevents the migration and sintering of the alloy and CeO_2 nanoparticles.

Kosari et al. [211] developed NHS-Ni/SiO_2 derived from nickel-silicate hollow spheres (NHS). Their study demonstrated that the shell thickness is closely related to the stability of the catalyst. Thick-shell Ni/SiO_2 exhibited whisker-like carbon growth, while thin-shell Ni/SiO_2 with maximized hollow interior space showed no coke formation during the DRM. The resistance to sintering of NHS-Ni/SiO_2 catalysts can be further improved by introducing ceria as a promoter [211]. Kim et al. [196] developed a coking-resistant yolk–shell Pt-NiCe@SiO_2 catalyst. The confined yolk–shell morphology of the catalyst prevented the aggregation and sintering of active metal particles, thereby suppressing carbon formation. The presence of Pt enhanced the metal–support interaction, improving the reducibility of the Ni species and reducing the likelihood of carbon formation. However, at high Pt loadings, the formation of Pt nanoparticles can lead to the deep cracking of the C-H species, resulting in coke formation. Wang et al. [195] proposed a different approach. They have indicated that a balance between shell thickness and porosity is necessary to prevent coking in small-sized yolk–shell Ni@SiO_2 catalysts (Figure 12). A thicker shell can prevent sintering and coking by acting as an armor and restricting the spatial growth of carbon. However, the dense shell also hinders the mass transfer to the internal active sites, thereby affecting the efficiency and stability of the catalyst. However, as the shell porosity decreases, the diffusion effects increase exponentially, leading to energy loss and reduced diffusion rates.

3.3.2. Perovskite-Derived Catalysts

Perovskite-type oxides have well-defined structures with the general formula ABO_3, where A is typically a rare earth or alkaline earth metal and B is a transition metal. Performance can be enhanced by substituting metal ions at the A- and B-sites. Substitution at site A typically involves enhancing the oxygen migration in the perovskite structure to suppress carbon deposition. In contrast, a dual-metal synergistic effect is achieved by adding a second metal at the B site, which often leads to an improved activity and stability of these catalysts.

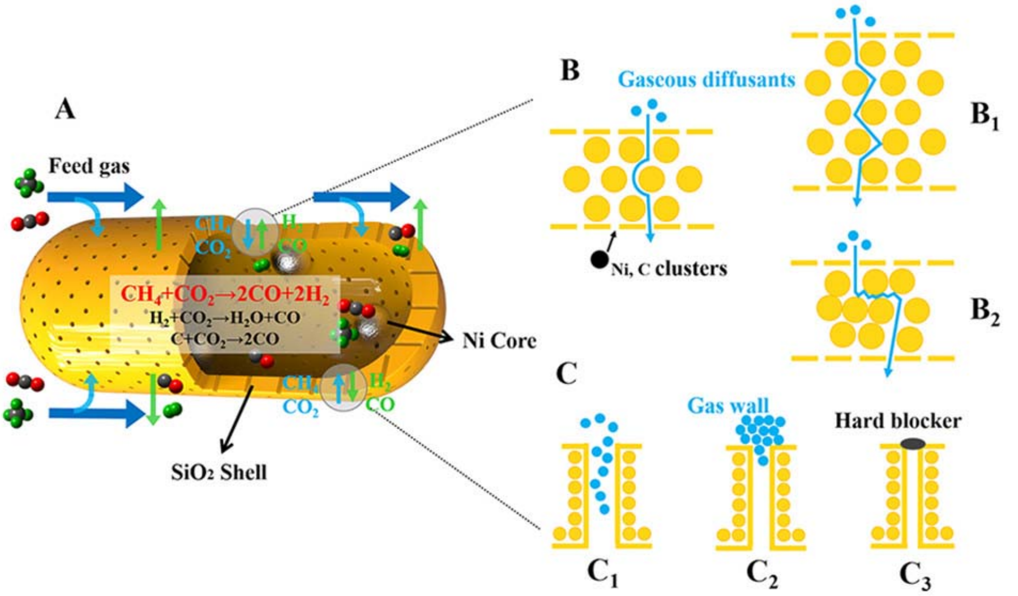

Figure 12. Schematic of the working principle of a nanoreactor for the yolk–shell Ni@SiO$_2$ catalysts concerning the shell diffusion effects. (**A**) Mass transfer exemplification across the shell. (**B**) Mechanism of gas (small) and solid (large) diffusant transport over the shell: (**B$_1$**) gas diffusant transport over the thick shell, (**B$_2$**) gas diffusant transport over the dense shell. (**C**) Mechanism of diffusant transport over the shell mesopore: (**C$_1$**) normal diffusant transport without interruption, (**C$_2$**) gas wall effect, (**C$_3$**) hard blocker effect [195]. The blue, cyan, and green arrows represent the feed stream, reactant stream into the nanoreactor, and product stream out of the nanoreactor, respectively. Copyright 2021, with permission from the American Chemical Society.

By controlling the morphological structure, the performance of LaNiO$_3$ catalysts can be regulated to achieve better catalytic effects. LaNiO$_3$ nanoparticles with rod-shaped and spherical morphologies have small depletion zones, allowing Ni to regenerate from the bulk material and achieving no carbon accumulation after a 100 h DRM [212]. In contrast, the cubic catalyst accumulated carbon and underwent sintering. Zhao et al. [213] prepared a Ni-La$_2$O$_2$CO$_3$ catalyst through an impregnation method containing two Ni species: isolated Ni nanoparticles and well-defined interfaces of Ni-La alloy. Carbon rapidly encapsulated the isolated Ni sites, forming carbon nanotubes that encased the Ni nanoparticles. However, no coking was observed at the Ni-La interfaces, even after 300 h of the DRM. LaNiO$_3$ prepared by citrate-gel combustion method exhibits an improved resistance to carbon deposition compared to the impregnation method and co-precipitation method due to the collapse of the Ni-based perovskite structure during hydrogen reduction and the formation of uniformly dispersed Ni nanoparticles on La$_2$O$_3$, allowing for a more optimized separation of CO from lanthanum carbonate for carbon removal [214]. On the LaNiO$_3$ supported by CeO$_2$-SiO$_2$, the oxidation state of CeO$_2$ can achieve a Ce^{4+} to Ce^{3+} redox cycle, which can both restrict the oxidation of Ni and inhibit the formation of nickel carbide by reacting with carbon due to its high oxygen migration rate [215]. As a result, the formation of carbon fibers was avoided. Bonmassar et al. [216] reported that LaNiO$_3$ exhibits polymorphism during the DRM process, including rhombic LaNiO$_3$, cubic LaNiO$_3$, monoclinic LaNiO$_{2.7}$, and monoclinic LaNiO$_{2.5}$. The lattice oxygen in these phases can activate the C-H bonds in CH$_4$, preventing coke formation. Additionally, the lattice oxygen can also combine with CO$_2$ to form monoclinic La$_2$O$_2$CO$_3$, which can further decompose into La$_2$O$_3$ and CO, thereby reducing carbon formation.

B-site substitution in LaNiO$_3$ perovskites has been extensively studied. Reduced perovskite LaNiO$_3$ catalysts modified with Co and Mn exhibit enhanced resistance to coking, which is attributed to the strong metal–support interactions mediated by Mn [217]. Mn substitution in LaNi$_{1-x}$Mn$_x$O$_3$ during spray pyrolysis creates a mesoporous structure and enhances oxygen migration, resulting in a significant reduction in carbon deposition and transformation from whiskers to an amorphous form [218]. Using glycine-assisted spray pyrolysis synthesis, $LaNi_{1-x}Mn_xO_3$ can also exhibit similar properties [219]. In $LaNi_xFe_{1-x}O_3$, the conversion rates of CH_4 and CO_2 increase with the increase in Ni and the decrease in Fe, with the optimal Ni/Fe ratio being 3:1 [220].

Moreover, the Ni/Fe ratio affects the syngas ratio [221]. Yao et al. demonstrated that the $PrBaMn_{1.6}Ni_{0.3}Fe_{0.1}O_{5+\delta}$ with uniform-sized Ni-Fe alloy exhibits negligible coking during a 40 h reaction under more severe coking conditions (14 bar) [222]. This is attributed to the addition of Fe, which stabilizes the O* species, facilitating CO_2 dissociation and promoting the reaction with the weakened adsorption of C* species. Moreover, the strong metal–support interactions resulted in a slower sintering rate, although the reaction rate was slightly lower. Partial Fe substitution in the $La_{0.9}Sr_{0.1}NiO_3$ perovskite catalyst enhanced its coking resistance [223]. The presence of Fe changed the reaction mechanism during the DRM. Mechanistic studies using isotopically labeled reactants and an in situ DRIFTS analysis indicated that on the $La_{0.9}Sr_{0.1}Ni_{0.5}Fe_{0.5}O_3$ catalyst, a lattice oxygen-mediated redox mechanism predominates, as shown in Figure 13. This mechanism facilitates the oxidation of the carbonaceous intermediates formed during methane decomposition, preventing coke formation. Furthermore, the stability and reversible regeneration of the $La_{0.9}Sr_{0.1}Ni_{0.5}Fe_{0.5}O_3$ perovskite phase played crucial roles in its resistance to coking. Even after reduction, the catalyst's perovskite structure is partially retained, and exposure to CO_2 or DRM feed gases leads to the further regeneration of the perovskite phase. The high oxygen migration rate and oxygen storage/release capacity of the $La_{0.9}Sr_{0.1}Ni_{0.5}Fe_{0.5}O_3$ perovskite aid in the oxidation of carbonaceous intermediates and prevent coke formation.

Bai et al. [224] reported that the coking resistance of Zr- and Ce-co-doped $La_2(CeZrNi)_2O_7$ catalysts showed a linear correlation with the number of oxygen vacancies in the catalyst. The size of the active metal is an essential factor affecting perovskite catalysts. Chai et al. [225] prepared a $La_{0.46}Sr_{0.34}Ti_{0.9}Ni_{0.1}O_3$ catalyst with a bimodal size distribution of Ni dopants consisting of small Ni particles (2.5 nm on average) and large Ni particles (14.5 nm on average). After a 100 h reaction, the catalyst exhibited an extremely high catalytic stability. In contrast, the catalyst containing only large Ni particles (finally at 14.5 nm on average) experienced rapid deactivation due to sintering and carbon deposition. The crystal structures of the perovskite precursors can influence the performance of the prepared catalysts. The $La(Co_xNi_{1-x})_{0.5}Fe_{0.5}O_3$ perovskite precursor is used to prepare Ni-Co/La_2O_3-$LaFeO_3$ catalysts [131]. The multivalent and spin states of the Co cations determine the perovskite configuration. Catalysts reduced from the orthorhombic perovskite precursors with $x = 0.10$ and 0.30 exhibit a significantly higher resistance to coking.

Similarly, A-site substitutions have also been extensively studied. Wei et al. [226] prepared a $La_{0.6}Sr_{0.2}Cr_{0.85}Ni_{0.15}$ catalyst by co-doping Sr and Ni cations at the A- and B-sites, respectively, of defective $LaCrO_3$. Adding Sr increased oxygen vacancies and basicity, thereby promoting CO_2 adsorption and dissociation. Additionally, the exsolved Ni particles exhibit strong interfacial interactions with the support, enhancing the resistance of the catalyst to carbon deposition. Dama et al. [227] studied $MZr_{0.8}Ni_{0.2}O_{3-\delta}$ (M = Ca, Sr, and Ba) catalysts doped with different alkaline-earth metals. Among them, the $SrZr_{0.8}Ni_{0.2}O_{3-\delta}$ and $BaZr_{0.8}Ni_{0.2}O_{3-\delta}$ catalysts exhibited rapid deactivation owing to the fast growth of graphite carbon and the formation of NiC_x species. However, $CaZr_{0.8}Ni_{0.2}O_{3-\delta}$ has more surface hydroxyl groups than other catalysts, showing better coke resistance. The presence of surface hydroxyl groups is responsible for the formation of hydroxyl species, which react with adsorbed hydrogen to produce water and desorb carbon monoxide. This reaction pathway prevents the accumulation and polymerization of carbonaceous intermediates, thereby facilitating the removal of carbon species. Doping Ce into Ni-loaded $PrCrO_3$ perovskites can significantly reduce the formation energy of oxygen vacancies, leading to a lower activation energy for oxygen ion migration within the perovskite structure [228]. This facilitates the rapid conversion of carbon to CO, the suppression of carbon deposition, and the enhancement of the catalyst stability. Bekheet et al. [183] studied the effects of different metals on the A (La, Ba) and B (Cu, Ni) site doping of Ruddlesden-Popper perovskite materials (La_2NiO_4). Ba doping leads to a highly stable calcium titanate structure without phase transitions in the temperature range of 25–800 °C. However, this also causes an increase in the Ni particle size and a lower amount of exsolved Ni species, resulting in a reduced catalytic activity. In contrast, the Cu-doped and undoped calcium titanate exhibited different degrees of phase transition during temperature variation. The Cu-Ni alloying enhances catalytic activity while maintaining a low Ni particle size, and it can also control the active carbonate species to suppress coking.

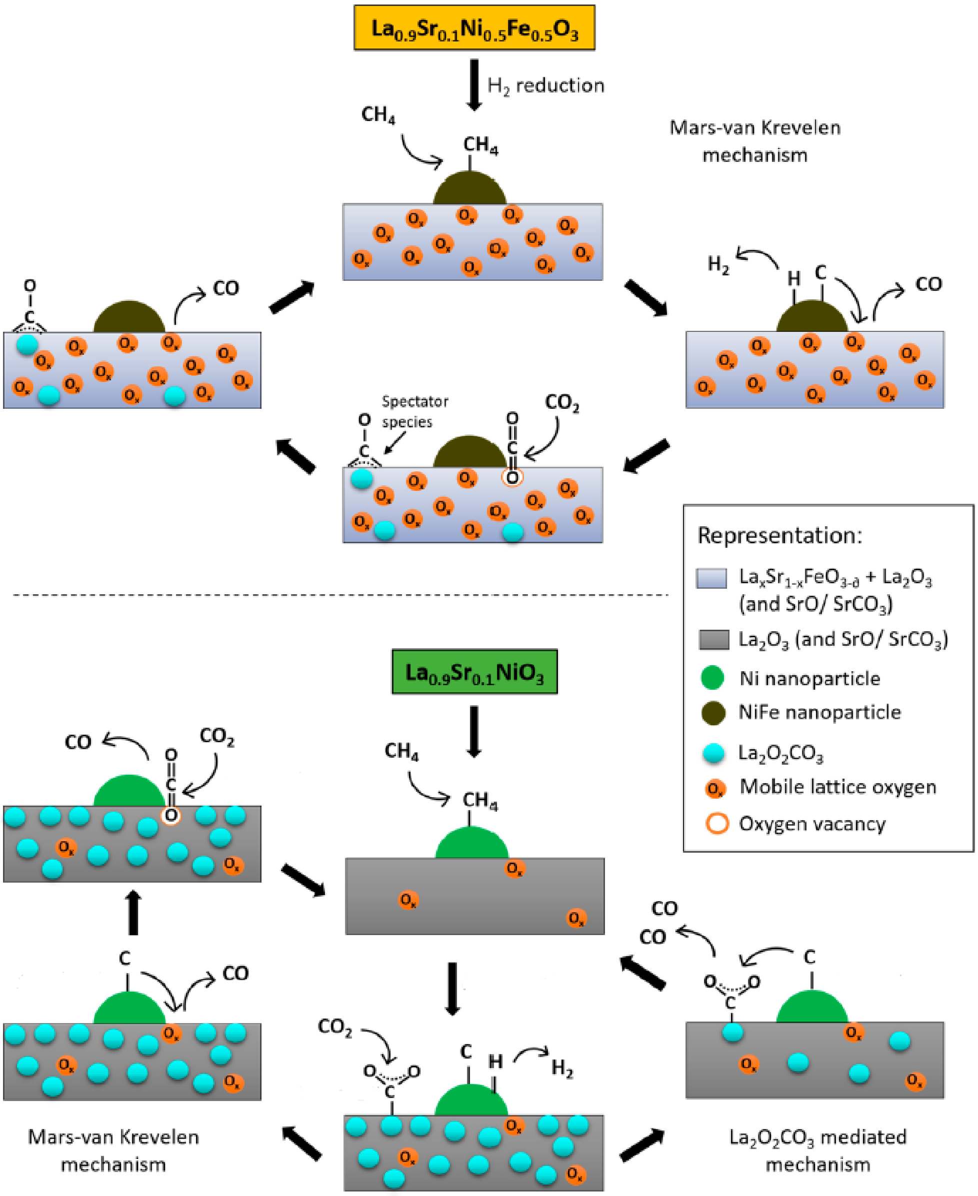

Figure 13. Schematic of the proposed reaction mechanism of the DRM on $La_{0.9}Sr_{0.1}NiO_3$- and $La_{0.9}Sr_{0.1}Ni_{0.5}Fe_{0.5}O_3$-derived catalysts [223]. Copyright 2020, with permission from the American Chemical Society.

3.3.3. Other Structured Catalysts

Ni-based catalysts with sandwich structures, where the active metal is confined to a narrow region, can effectively suppress the aggregation and carbon deposition of active nanoparticles owing to the confinement effect of the supports [192,229,230]. Qu et al. [201] layered original kaolin into nanoplates rich in etch pits and combined them with Ni particles to prepare a sandwich-structured Ni-NKaol catalyst. Owing to the confinement and isolation effects of the sandwich structure, the generated carbon deposits appeared as filamentous carbon, which had no impact on the catalytic activity and stability. In contrast, for supported Ni-based catalysts, the formation of encapsulated carbon can lead to catalyst deactivation.

Bu et al. [62] developed an efficient and stable NiMA (MA = Mg, Al)-BN-M-R catalyst derived from layered double hydroxides (LDHs). The constraint effect and strong metal–support interaction between h-BN and the LDHs interface not only inhibits the sintering of Ni particles but also improves the adsorption and activation ability of the reactants, which is beneficial for coke removal and enhances coking resistance. Kim et al. [231] employed an exsolution method to incorporate Co into Ni/$MgAl_2O_4$ catalysts. When the Ni/Co ratio is 4:1, the dominant pathway for the anti-coking formate-intermediate reaction leads to a coke deposition rate of 0.2 μg coke·g_{cat}.$^{-1}$ h^{-1}. Dou et al. [191] prepared a sandwiched core–shell catalyst, SiO_2@Ni@ZrO_2, by encapsulating Ni nanoparticles between a silica core and a zirconia shell using the precipitation method. The catalyst exhibits high CO_2 adsorption capacity and low dissociation barrier, producing an excellent coke resistance and superior catalytic performance. Wang et al. developed a coke-resistant Ni@S-2 using a one-pot approach in which Ni nanoparticles were sandwiched within a peasecod-like structured microporous silicalite-2 (Figure 14), where their size could be precisely controlled and the migration of Ni nanoparticles was restricted [42]. Consequently, the catalyst exhibited excellent carbon resistance.

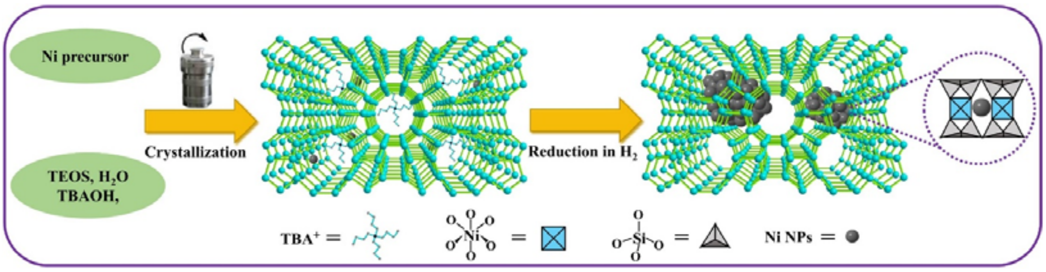

Figure 14. Schematic of Ni@S-2 catalyst via a facile one-pot approach [42]. Copyright 2021, with permission from Elsevier.

4. Summary and Outlook

The dry reforming of methane (DRM) over Ni-based catalysts presents a promising pathway for transforming two major greenhouse gases (methane and carbon dioxide) into valuable syngas. However, coke management continues to be a critical concern in the industrial application of DRM technology. The carbon deposition resulting from methane cracking and the Boudouard reaction lead to catalyst deactivation, ultimately limiting the lifetime of the catalyst and hindering its widespread implementation. To address this issue, extensive research has been conducted to develop effective strategies for mitigating coke formation and prolonging catalyst activity. Various carbon management approaches, including anti-coking catalyst optimization, process parameter adjustments, and reactor design enhancements, have been explored to reduce or prevent coke formation during the DRM. In this review, we elucidate the recent design strategies for anti-coking catalysts, including support optimization, bimetallic catalyst design, and structured catalyst development.

The choice of support for Ni-based catalysts in the DRM is pivotal for enhancing their ability to resist carbon deposition. In the design of catalysts, various parameters, including the SMSI, support surface acidity/basicity, morphology, and redox properties, should be comprehensively considered. Doping with a secondary metal results in a notable improvement in the carbon-resistance performance of Ni catalysts through surface modification, alloy effects, and synergistic interactions. However, the economic feasibility of using this additional metal must be considered. From this point of view, it is desirable to reduce the use of precious metals to a minimum, even in the case of alloy catalysts.

Constructing catalysts with specific morphologies or well-defined structures can achieve both the confinement effect, which reduces the size of the Ni particles to provide more active sites, and limits the migration and dispersion of active Ni to avoid metal sintering. In future catalyst designs, careful consideration and the thorough exploration of the intrinsic connections among these three strategies should be emphasized, rather than a simplistic superposition or isolated application. This entails approaching the design of new catalysts systematically and comprehensively integrating these strategies to achieve more synergistic and comprehensive effects.

The future development of the DRM can be considered in the following outlook for scholarly reference: Coke formation is one of the many factors that lead to catalyst deactivation, including sintering and poisoning. Therefore, an advanced catalyst design should consider various limiting factors, be suitable for more severe reaction conditions, and reduce reactant requirements. Using intelligent technologies (e.g., machine learning [232], artificial intelligence [233]), and density functional theory (DFT) [234] to assist catalyst design is a promising approach. For instance, descriptors obtained through DFT or experimental data play a crucial role in efficiently screening massive catalytic materials for the DRM, and machine learning and artificial neural networks can predict key catalytic performance indicators, such as CH_4 and CO_2 conversion, the synthesis gas ratio, and carbon deposition, thus contributing to the reduction of manual costs, acceleration of the catalyst development processes, and promotion of the widespread application of catalyst technology under more severe reaction conditions.

Reaction and deactivation mechanisms limit the comprehensive elucidation of the development of DRM technology owing to harsh reaction conditions. Incorporating more advanced in situ characterization techniques is crucial for gaining real-time insights and guiding the progress of DRM technology to overcome these limitations. With a comprehensive understanding of the DRM reactions, researchers can develop improved catalysts and efficient coke-management strategies.

Owing to the inevitable high-temperature environment associated with thermally driven catalytic systems, which leads to a high energy consumption and catalyst carbon deposition, new catalytic technologies, including built-in electric-field-assisted photocatalysis [235], nonthermal plasma technology [236], and Joule heating [237], should be considered. The incorporation of an internal electric field can enhance the separation and transport dynamics of charge carriers in the photocatalytic DRM, thereby further improving the photocatalytic efficiency. The plasma-assisted DRM is an efficient process capable of activating CH_4 and CO_2 at low temperatures and pressures. Joule heating is a promising electrification method. In addition to reducing CO_2 emissions through the substitution of fuel combustion, Joule heating-driven catalytic processes can be intensified by designing compact reactors, thereby mitigating the inherent heat transfer limitations that affect the DRM process.

Currently, most reports on catalyst preparation routes are limited to the laboratory scale, leading to complex and difficult-to-reproduce preparation processes and limiting the industrial application of this technology. Therefore, ensuring a stable supply and mass production of high-quality catalysts is key to promoting the practical application of this technology.

Author Contributions: Conceptualization, E.D.P.; writing—original draft preparation, Z.X.; writing—review and editing, E.D.P.; supervision, project administration, and funding acquisition, E.D.P. All authors have read and agreed to the published version of the manuscript.

Funding: This work was supported by the C1 Gas Refinery Program of the National Research Foundation (NRF) of Korea and funded by the Ministry of Science, ICT, and Future Planning (2015M3D3A1A01064899). This research was also supported by the H2KOREA funded by the Ministry of Education (2002Hydrogen fuel cell-002, Innovative Human Resource Development Project for Hydrogen Fuel Cells).

Data Availability Statement: No new data were created or analyzed in this study. Data sharing is not applicable to this article.

Acknowledgments: We thank Alexander Huang (adh9@rice.edu), Department of Chemistry, Rice University, for the assistance with data collection.

Conflicts of Interest: The authors declare no conflicts of interest.

References

1. Carley, S.; Konisky, D.M. The justice and equity implications of the clean energy transition. *Nat. Energy* **2020**, *5*, 569–577. [CrossRef]
2. Abe, J.O.; Popoola, A.P.I.; Ajenifuja, E.; Popoola, O.M. Hydrogen energy, economy and storage: Review and recommendation. *Int. J. Hydrogen Energy* **2019**, *44*, 15072–15086. [CrossRef]
3. Chen, J.M. Carbon neutrality: Toward a sustainable future. *Innovation* **2021**, *2*, 100127. [CrossRef] [PubMed]
4. Song, C. Global challenges and strategies for control, conversion and utilization of CO_2 for sustainable development involving energy, catalysis, adsorption and chemical processing. *Catal. Today* **2006**, *115*, 2–32. [CrossRef]
5. Hepburn, C.; Adlen, E.; Beddington, J.; Carter, E.A.; Fuss, S.; Mac Dowell, N.; Minx, J.C.; Smith, P.; Williams, C.K. The technological and economic prospects for CO_2 utilization and removal. *Nature* **2019**, *575*, 87–97. [CrossRef] [PubMed]
6. Koolen, C.D.; Luo, W.; Züttel, A. From Single Crystal to Single Atom Catalysts: Structural Factors Influencing the Performance of Metal Catalysts for CO_2 Electroreduction. *ACS Catal.* **2023**, *13*, 948–973. [CrossRef]
7. Zhang, J.; Pham, T.H.M.; Ko, Y.; Li, M.; Yang, S.; Koolen, C.D.; Zhong, L.; Luo, W.; Züttel, A. Tandem effect of Ag@C@Cu catalysts enhances ethanol selectivity for electrochemical CO_2 reduction in flow reactors. *Cell Rep. Phys. Sci.* **2022**, *3*, 100949. [CrossRef]
8. Wang, M.; Luo, L.; Wang, C.; Du, J.; Li, H.; Zeng, J. Heterogeneous Catalysts toward CO_2 Hydrogenation for Sustainable Carbon Cycle. *Acc. Mater. Res.* **2022**, *3*, 565–571. [CrossRef]
9. Saunois, M.; Stavert, A.R.; Poulter, B.; Bousquet, P.; Canadell, J.G.; Jackson, R.B.; Raymond, P.A.; Dlugokencky, E.J.; Houweling, S.; Patra, P.K. The global methane budget 2000–2017. *Earth Syst. Sci. Data* **2020**, *12*, 1561–1623. [CrossRef]
10. Dummer, N.F.; Willock, D.J.; He, Q.; Howard, M.J.; Lewis, R.J.; Qi, G.; Taylor, S.H.; Xu, J.; Bethell, D.; Kiely, C.J.; et al. Methane Oxidation to Methanol. *Chem. Rev.* **2023**, *123*, 6359–6411. [CrossRef]
11. Li, X.; Wang, C.; Tang, J. Methane transformation by photocatalysis. *Nat. Rev. Mater.* **2022**, *7*, 617–632. [CrossRef]
12. Meng, X.; Cui, X.; Rajan, N.P.; Yu, L.; Deng, D.; Bao, X. Direct Methane Conversion under Mild Condition by Thermo-, Electro-, or Photocatalysis. *Chem* **2019**, *5*, 2296–2325. [CrossRef]
13. McConnachie, M.; Konarova, M.; Smart, S. Literature review of the catalytic pyrolysis of methane for hydrogen and carbon production. *Int. J. Hydrogen Energy* **2023**, *48*, 25660–25682. [CrossRef]
14. Koo, C.W.; Rosenzweig, A.C. Biochemistry of aerobic biological methane oxidation. *Chem. Soc. Rev.* **2021**, *50*, 3424–3436. [CrossRef]
15. Zhang, H.; Sun, Z.; Hu, Y.H. Steam reforming of methane: Current states of catalyst design and process upgrading. *Renew. Sustain. Energy Rev.* **2021**, *149*, 111330. [CrossRef]
16. Parsapur, R.K.; Chatterjee, S.; Huang, K.-W. The Insignificant Role of Dry Reforming of Methane in CO_2 Emission Relief. *ACS Energy Lett.* **2020**, *5*, 2881–2885. [CrossRef]
17. Abdulrasheed, A.; Jalil, A.A.; Gambo, Y.; Ibrahim, M.; Hambali, H.U.; Shahul Hamid, M.Y. A review on catalyst development for dry reforming of methane to syngas: Recent advances. *Renew. Sustain. Energy Rev.* **2019**, *108*, 175–193. [CrossRef]
18. Yentekakis, I.V.; Panagiotopoulou, P.; Artemakis, G. A review of recent efforts to promote dry reforming of methane (DRM) to syngas production via bimetallic catalyst formulations. *Appl. Catal. B Environ.* **2021**, *296*, 120210. [CrossRef]
19. Shi, C.; Wang, S.; Ge, X.; Deng, S.; Chen, B.; Shen, J. A review of different catalytic systems for dry reforming of methane: Conventional catalysis-alone and plasma-catalytic system. *J. CO_2 Util.* **2021**, *46*, 101462. [CrossRef]
20. Khodakov, A.Y.; Chu, W.; Fongarland, P. Advances in the Development of Novel Cobalt Fischer−Tropsch Catalysts for Synthesis of Long-Chain Hydrocarbons and Clean Fuels. *Chem. Rev.* **2007**, *107*, 1692–1744. [CrossRef]
21. Gao, Y.; Jiang, J.; Meng, Y.; Yan, F.; Aihemaiti, A. A review of recent developments in hydrogen production via biogas dry reforming. *Energy Convers. Manag.* **2018**, *171*, 133–155. [CrossRef]
22. Jung, S.; Lee, J.; Moon, D.H.; Kim, K.-H.; Kwon, E.E. Upgrading biogas into syngas through dry reforming. *Renew. Sustain. Energy Rev.* **2021**, *143*, 110949. [CrossRef]
23. Aramouni, N.A.K.; Touma, J.G.; Tarboush, B.A.; Zeaiter, J.; Ahmad, M.N. Catalyst design for dry reforming of methane: Analysis review. *Renew. Sustain. Energy Rev.* **2018**, *82*, 2570–2585. [CrossRef]
24. Wang, S.; Lu, G.Q.; Millar, G.J. Carbon Dioxide Reforming of Methane To Produce Synthesis Gas over Metal-Supported Catalysts: State of the Art. *Energy Fuels* **1996**, *10*, 896–904. [CrossRef]
25. Pati, S.; Das, S.; Dewangan, N.; Jangam, A.; Kawi, S. Facile integration of core–shell catalyst and Pd-Ag membrane for hydrogen production from low-temperature dry reforming of methane. *Fuel* **2023**, *333*, 126433. [CrossRef]
26. Kwon, H.; Kim, T.; Song, S. Dry reforming of methane in a rotating gliding arc plasma: Improving efficiency and syngas cost by quenching product gas. *J. CO_2 Util.* **2023**, *70*, 102448. [CrossRef]

27. Song, Y.; Ozdemir, E.; Ramesh, S.; Adishev, A.; Subramanian, S.; Harale, A.; Albuali, M.; Fadhel, B.A.; Jamal, A.; Moon, D.; et al. Dry reforming of methane by stable Ni–Mo nanocatalysts on single-crystalline MgO. *Science* **2020**, *367*, 777–781. [CrossRef]
28. Buelens, L.C.; Galvita, V.V.; Poelman, H.; Detavernier, C.; Marin, G.B. Super-dry reforming of methane intensifies CO_2 utilization via Le Chatelier's principle. *Science* **2016**, *354*, 449–452. [CrossRef]
29. Zhu, Q.; Zhou, H.; Wang, L.; Wang, L.; Wang, C.; Wang, H.; Fang, W.; He, M.; Wu, Q.; Xiao, F.-S. Enhanced CO_2 utilization in dry reforming of methane achieved through nickel-mediated hydrogen spillover in zeolite crystals. *Nat. Catal.* **2022**, *5*, 1030–1037. [CrossRef]
30. Akri, M.; Zhao, S.; Li, X.; Zang, K.; Lee, A.F.; Isaacs, M.A.; Xi, W.; Gangarajula, Y.; Luo, J.; Ren, Y.; et al. Atomically dispersed nickel as coke-resistant active sites for methane dry reforming. *Nat. Commun.* **2019**, *10*, 5181. [CrossRef]
31. Baharudin, L.; Rahmat, N.; Othman, N.H.; Shah, N.; Syed-Hassan, S.S.A. Formation, control, and elimination of carbon on Ni-based catalyst during CO_2 and CH_4 conversion via dry reforming process: A review. *J. CO_2 Util.* **2022**, *61*, 102050. [CrossRef]
32. Grams, J.; Ruppert, A.M. Catalyst Stability—Bottleneck of Efficient Catalytic Pyrolysis. *Catalysts* **2021**, *11*, 265. [CrossRef]
33. Hambali, H.U.; Jalil, A.A.; Abdulrasheed, A.A.; Siang, T.J.; Gambo, Y.; Umar, A.A. Zeolite and clay based catalysts for CO_2 reforming of methane to syngas: A review. *Int. J. Hydrogen Energy* **2022**, *47*, 30759–30787. [CrossRef]
34. Yousefi, M.; Donne, S. Technical challenges for developing thermal methane cracking in small or medium scales to produce pure hydrogen—A review. *Int. J. Hydrogen Energy* **2022**, *47*, 699–727. [CrossRef]
35. Fakeeha, A.H.; Patel, R.; El Hassan, N.; Al-Zahrani, S.A.; Al-Awadi, A.S.; Frusteri, L.; Bayahia, H.; Alharth, A.I.; Al-Fatesh, A.S.; Kumar, R. Holmium promoted yttria-zirconia supported Ni catalyst for H_2 production via dry reforming of methane. *Int. J. Hydrogen Energy* **2022**, *47*, 38242–38257. [CrossRef]
36. Deng, J.; Bu, K.; Shen, Y.; Zhang, X.; Zhang, J.; Faungnawakij, K.; Zhang, D. Cooperatively enhanced coking resistance via boron nitride coating over Ni-based catalysts for dry reforming of methane. *Appl. Catal. B Environ.* **2022**, *302*, 120859. [CrossRef]
37. Rosli, S.N.A.; Abidin, S.Z.; Osazuwa, O.U.; Fan, X.; Jiao, Y. The effect of oxygen mobility/vacancy on carbon gasification in nano catalytic dry reforming of methane: A review. *J. CO_2 Util.* **2022**, *63*, 102109. [CrossRef]
38. Pakhare, D.; Spivey, J. A review of dry (CO_2) reforming of methane over noble metal catalysts. *Chem. Soc. Rev.* **2014**, *43*, 7813–7837. [CrossRef]
39. Bartholomew, C.H. Carbon Deposition in Steam Reforming and Methanation. *Catal. Rev.* **1982**, *24*, 67–112. [CrossRef]
40. Wang, J.; Fu, Y.; Kong, W.; Li, S.; Yuan, C.; Bai, J.; Chen, X.; Zhang, J.; Sun, Y. Investigation of Atom-Level Reaction Kinetics of Carbon-Resistant Bimetallic NiCo-Reforming Catalysts: Combining Microkinetic Modeling and Density Functional Theory. *ACS Catal.* **2022**, *12*, 4382–4393. [CrossRef]
41. Kong, W.; Fu, Y.; Shi, L.; Li, S.; Vovk, E.; Zhou, X.; Si, R.; Pan, B.; Yuan, C.; Li, S.; et al. Nickel nanoparticles with interfacial confinement mimic noble metal catalyst in methane dry reforming. *Appl. Catal. B Environ.* **2021**, *285*, 119837. [CrossRef]
42. Wang, J.; Fu, Y.; Kong, W.; Jin, F.; Bai, J.; Zhang, J.; Sun, Y. Design of a carbon-resistant Ni@S-2 reforming catalyst: Controllable Ni nanoparticles sandwiched in a peasecod-like structure. *Appl. Catal. B Environ.* **2021**, *282*, 119546. [CrossRef]
43. Oh, K.H.; Lee, J.H.; Kim, K.; Lee, H.-K.; Kang, S.W.; Yang, J.-I.; Park, J.-H.; Hong, C.S.; Kim, B.-H.; Park, J.C. A new automated synthesis of a coke-resistant Cs-promoted Ni-supported nanocatalyst for sustainable dry reforming of methane. *J. Mater. Chem. A* **2023**, *11*, 1666–1675. [CrossRef]
44. Fakeeha, A.H.; Al-Fatesh, A.S.; Srivastava, V.K.; Ibrahim, A.A.; Abahussain, A.A.M.; Abu-Dahrieh, J.K.; Alotibi, M.F.; Kumar, R. Hydrogen Production from Gadolinium-Promoted Yttrium-Zirconium-Supported Ni Catalysts through Dry Methane Reforming. *ACS Omega* **2023**, *8*, 22108–22120. [CrossRef] [PubMed]
45. Ekeoma, B.C.; Yusuf, M.; Johari, K.; Abdullah, B. Mesoporous silica supported Ni-based catalysts for methane dry reforming: A review of recent studies. *Int. J. Hydrogen Energy* **2022**, *47*, 41596–41620. [CrossRef]
46. Vogt, C.; Weckhuysen, B.M. The concept of active site in heterogeneous catalysis. *Nat. Rev. Chem.* **2022**, *6*, 89–111. [CrossRef] [PubMed]
47. Wang, Z.; Cao, X.-M.; Zhu, J.; Hu, P. Activity and coke formation of nickel and nickel carbide in dry reforming: A deactivation scheme from density functional theory. *J. Catal.* **2014**, *311*, 469–480. [CrossRef]
48. Wang, D.; Littlewood, P.; Marks, T.J.; Stair, P.C.; Weitz, E. Coking Can Enhance Product Yields in the Dry Reforming of Methane. *ACS Catal.* **2022**, *12*, 8352–8362. [CrossRef]
49. Guo, Z.; Chen, S.; Yang, B. Promoted coke resistance of Ni by surface carbon for the dry reforming of methane. *iScience* **2023**, *26*, 106237. [CrossRef]
50. Shen, D.; Wang, J.; Bai, Y.; Lyu, S.; Zhang, Y.; Li, J.; Li, L.; Wang, G. Carbon-confined Ni based catalyst by auto-reduction for low-temperature dry reforming of methane. *Fuel* **2023**, *339*, 127409. [CrossRef]
51. van Deelen, T.W.; Hernández Mejía, C.; de Jong, K.P. Control of metal-support interactions in heterogeneous catalysts to enhance activity and selectivity. *Nat. Catal.* **2019**, *2*, 955–970. [CrossRef]
52. Li, Y.; Zhang, Y.; Qian, K.; Huang, W. Metal–Support Interactions in Metal/Oxide Catalysts and Oxide–Metal Interactions in Oxide/Metal Inverse Catalysts. *ACS Catal.* **2022**, *12*, 1268–1287. [CrossRef]
53. Pu, T.; Zhang, W.; Zhu, M. Engineering Heterogeneous Catalysis with Strong Metal–Support Interactions: Characterization, Theory and Manipulation. *Angew. Chem. Int. Ed.* **2023**, *62*, e202212278. [CrossRef] [PubMed]
54. Hu, S.; Li, W.-X. Sabatier principle of metal-support interaction for design of ultrastable metal nanocatalysts. *Science* **2021**, *374*, 1360–1365. [CrossRef]

55. Frey, H.; Beck, A.; Huang, X.; van Bokhoven, J.A.; Willinger, M.G. Dynamic interplay between metal nanoparticles and oxide support under redox conditions. *Science* **2022**, *376*, 982–987. [CrossRef]
56. Al-Fatesh, A.S.; Patel, N.; Fakeeha, A.H.; Alotibi, M.F.; Alreshaidan, S.B.; Kumar, R. Reforming of methane: Effects of active metals, supports, and promoters. *Catal. Rev. Sci. Eng.* **2023**, 1–99. [CrossRef]
57. Ahmad, Y.H.; Mohamed, A.T.; El-Sayed, H.A.; Kumar, A.; Al-Qaradawi, S.Y. Design of Ni/La_2O_3 catalysts for dry reforming of methane: Understanding the impact of synthesis methods. *Int. J. Hydrogen Energy* **2022**, *47*, 41294–41309. [CrossRef]
58. Ahn, S.-Y.; Jang, W.-J.; Shim, J.-O.; Jeon, B.-H.; Roh, H.-S. CeO_2-based oxygen storage capacity materials in environmental and energy catalysis for carbon neutrality: Extended application and key catalytic properties. *Catal. Rev. Sci. Eng.* **2023**, 1–84. [CrossRef]
59. Bahari, M.B.; Setiabudi, H.D.; Duy Nguyen, T.; Phuong, P.T.T.; Duc Truong, Q.; Abdul Jalil, A.; Ainirazali, N.; Vo, D.-V.N. Insight into the influence of rare-earth promoter (CeO_2, La_2O_3, Y_2O_3, and Sm_2O_3) addition toward methane dry reforming over Co/mesoporous alumina catalysts. *Chem. Eng. Sci.* **2020**, *228*, 115967. [CrossRef]
60. Scheiber, P.; Fidler, M.; Dulub, O.; Schmid, M.; Diebold, U.; Hou, W.; Aschauer, U.; Selloni, A. (Sub)Surface Mobility of Oxygen Vacancies at the TiO_2 Anatase (101) Surface. *Phys. Rev. Lett.* **2012**, *109*, 136103. [CrossRef] [PubMed]
61. Onn, T.M.; Zhang, S.; Arroyo-Ramirez, L.; Chung, Y.-C.; Graham, G.W.; Pan, X.; Gorte, R.J. Improved Thermal Stability and Methane-Oxidation Activity of Pd/Al_2O_3 Catalysts by Atomic Layer Deposition of ZrO_2. *ACS Catal.* **2015**, *5*, 5696–5701. [CrossRef]
62. Bu, K.; Kuboon, S.; Deng, J.; Li, H.; Yan, T.; Chen, G.; Shi, L.; Zhang, D. Methane dry reforming over boron nitride interface-confined and LDHs-derived Ni catalysts. *Appl. Catal. B Environ.* **2019**, *252*, 86–97. [CrossRef]
63. Tuci, G.; Liu, Y.; Rossin, A.; Guo, X.; Pham, C.; Giambastiani, G.; Pham-Huu, C. Porous Silicon Carbide (SiC): A Chance for Improving Catalysts or Just Another Active-Phase Carrier? *Chem. Rev.* **2021**, *121*, 10559–10665. [CrossRef]
64. Shen, D.; Huo, M.; Li, L.; Lyu, S.; Wang, J.; Wang, X.; Zhang, Y.; Li, J. Effects of alumina morphology on dry reforming of methane over Ni/Al_2O_3 catalysts. *Catal. Sci. Technol.* **2020**, *10*, 510–516. [CrossRef]
65. Gholizadeh, F.; Izadbakhsh, A.; Huang, J.; Zi-Feng, Y. Catalytic performance of cubic ordered mesoporous alumina supported nickel catalysts in dry reforming of methane. *Microporous Mesoporous Mater.* **2021**, *310*, 110616. [CrossRef]
66. Ali, S.; Khader, M.M.; Almarri, M.J.; Abdelmoneim, A.G. Ni-based nano-catalysts for the dry reforming of methane. *Catal. Today* **2020**, *343*, 26–37. [CrossRef]
67. Lu, M.; Zhang, X.; Deng, J.; Kuboon, S.; Faungnawakij, K.; Xiao, S.; Zhang, D. Coking-resistant dry reforming of methane over BN–nanoceria interface-confined Ni catalysts. *Catal. Sci. Technol.* **2020**, *10*, 4237–4244. [CrossRef]
68. Ma, Q.; Han, Y.; Wei, Q.; Makpal, S.; Gao, X.; Zhang, J.; Zhao, T.-S. Stabilizing Ni on bimodal mesoporous-macroporous alumina with enhanced coke tolerance in dry reforming of methane to syngas. *J. CO_2 Util.* **2020**, *35*, 288–297. [CrossRef]
69. Al-Swai, B.M.; Osman, N.; Alnarabiji, M.S.; Adesina, A.A.; Abdullah, B. Syngas Production via Methane Dry Reforming over Ceria–Magnesia Mixed Oxide-Supported Nickel Catalysts. *Ind. Eng. Chem. Res.* **2019**, *58*, 539–552. [CrossRef]
70. Vasiliades, M.A.; Djinović, P.; Davlyatova, L.F.; Pintar, A.; Efstathiou, A.M. Origin and reactivity of active and inactive carbon formed during DRM over Ni/$Ce_{0.38}Zr_{0.62}O_{2-\delta}$ studied by transient isotopic techniques. *Catal. Today* **2018**, *299*, 201–211. [CrossRef]
71. Chong, C.C.; Cheng, Y.W.; Bukhari, S.N.; Setiabudi, H.D.; Jalil, A.A. Methane dry reforming over Ni/fibrous SBA-15 catalysts: Effects of support morphology (rod-liked F-SBA-15 and dendritic DFSBA-15). *Catal. Today* **2021**, *375*, 245–257. [CrossRef]
72. Jin, F.; Fu, Y.; Kong, W.; Wang, J.; Cai, F.; Yuan, C.; Pan, B.; Zhang, J.; Sun, Y. Stable Trimetallic NiFeCu Catalysts with High Carbon Resistance for Dry Reforming of Methane. *ChemPlusChem* **2020**, *85*, 1120–1128. [CrossRef]
73. Bawah, A.-R.; Malaibari, Z.O.; Muraza, O. Syngas production from CO_2 reforming of methane over Ni supported on hierarchical silicalite-1 fabricated by microwave-assisted hydrothermal synthesis. *Int. J. Hydrogen Energy* **2018**, *43*, 13177–13189. [CrossRef]
74. Danghyan, V.; Calderon Novoa, S.; Mukasyan, A.; Wolf, E.E. Pressure dilution, a new method to prepare a stable Ni/fumed silica catalyst for the dry reforming of methane. *Appl. Catal. B Environ.* **2018**, *234*, 178–186. [CrossRef]
75. Hambali, H.U.; Jalil, A.A.; Abdulrasheed, A.A.; Siang, T.J.; Abdullah, T.A.T.; Ahmad, A.; Vo, D.-V.N. Fibrous spherical Ni-M/ZSM-5 (M: Mg, Ca, Ta, Ga) catalysts for methane dry reforming: The interplay between surface acidity-basicity and coking resistance. *Int. J. Energy Res.* **2020**, *44*, 5696–5712. [CrossRef]
76. Chang, K.; Zhang, H.; Cheng, M.-j.; Lu, Q. Application of Ceria in CO_2 Conversion Catalysis. *ACS Catal.* **2020**, *10*, 613–631. [CrossRef]
77. Muravev, V.; Parastaev, A.; van den Bosch, Y.; Ligt, B.; Claes, N.; Bals, S.; Kosinov, N.; Hensen, E.J.M. Size of cerium dioxide support nanocrystals dictates reactivity of highly dispersed palladium catalysts. *Science* **2023**, *380*, 1174–1179. [CrossRef] [PubMed]
78. Al-Fatesh, A.S.; Arafat, Y.; Kasim, S.O.; Ibrahim, A.A.; Abasaeed, A.E.; Fakeeha, A.H. In situ auto-gasification of coke deposits over a novel Ni-Ce/W-Zr catalyst by sequential generation of oxygen vacancies for remarkably stable syngas production via CO_2-reforming of methane. *Appl. Catal. B Environ.* **2021**, *280*, 119445. [CrossRef]
79. Damaskinos, C.M.; Zavašnik, J.; Djinović, P.; Efstathiou, A.M. Dry reforming of methane over Ni/$Ce_{0.8}Ti_{0.2}O_{2-\delta}$: The effect of Ni particle size on the carbon pathways studied by transient and isotopic techniques. *Appl. Catal. B Environ.* **2021**, *296*, 120321. [CrossRef]

80. da Fonseca, R.O.; Ponseggi, A.R.; Rabelo-Neto, R.C.; Simões, R.C.C.; Mattos, L.V.; Noronha, F.B. Controlling carbon formation over Ni/CeO_2 catalyst for dry reforming of CH_4 by tuning Ni crystallite size and oxygen vacancies of the support. *J. CO_2 Util.* **2022**, *57*, 101880. [CrossRef]
81. Wang, Y.; Zhang, R.; Yan, B. Ni/$Ce_{0.9}Eu_{0.1}O_{1.95}$ with enhanced coke resistance for dry reforming of methane. *J. Catal.* **2022**, *407*, 77–89. [CrossRef]
82. Ding, X.; Yang, Y.; Li, Z.; Huang, P.; Liu, X.; Guo, Y.; Wang, Y. Engineering a Nickel–Oxygen Vacancy Interface for Enhanced Dry Reforming of Methane: A Promoted Effect of CeO_2 Introduction into Ni/MgO. *ACS Catal.* **2023**, *13*, 15535–15545. [CrossRef]
83. Tsoukalou, A.; Imtiaz, Q.; Kim, S.M.; Abdala, P.M.; Yoon, S.; Müller, C.R. Dry-reforming of methane over bimetallic Ni–M/La_2O_3 (M=Co, Fe): The effect of the rate of $La_2O_2CO_3$ formation and phase stability on the catalytic activity and stability. *J. Catal.* **2016**, *343*, 208–214. [CrossRef]
84. Zeng, F.; Wei, B.; Lan, D.; Ge, J. Highly Dispersed Ni_xGa_y Catalyst and La_2O_3 Promoter Supported by LDO Nanosheets for Dry Reforming of Methane: Synergetic Catalysis by Ni, Ga, and La_2O_3. *Langmuir* **2021**, *37*, 9744–9754. [CrossRef]
85. Song, J.; Duan, X.; Zhang, W. Methane dry reforming over mesoporous La_2O_3 supported Ni catalyst for syngas production. *Microporous Mesoporous Mater.* **2021**, *310*, 110587. [CrossRef]
86. Haug, L.; Thurner, C.; Bekheet, M.F.; Bischoff, B.; Gurlo, A.; Kunz, M.; Sartory, B.; Penner, S.; Klötzer, B. Zirconium Carbide Mediates Coke-Resistant Methane Dry Reforming on Nickel-Zirconium Catalysts. *Angew. Chem. Int. Ed.* **2022**, *61*, e202213249. [CrossRef]
87. Haug, L.; Thurner, C.; Bekheet, M.F.; Ploner, K.; Bischoff, B.; Gurlo, A.; Kunz, M.; Sartory, B.; Penner, S.; Klötzer, B. Pivotal Role of Ni/ZrO_2 Phase Boundaries for Coke-Resistant Methane Dry Reforming Catalysts. *Catalysts* **2023**, *13*, 804. [CrossRef]
88. Liu, Y.; Zheng, J.; Yan, T.; Deng, J.; Fang, J.; Zhang, D. Emergent Ni catalysts induced by nitride-to-oxide transformation for coking and sintering resistant dry reforming of methane. *New J. Chem.* **2023**, *47*, 10604–10612. [CrossRef]
89. Wang, Y.; Li, L.; Li, G.; Zhao, Q.; Wu, X.S.; Wang, Y.; Sun, Y.; Hu, C. Synergy of Oxygen Vacancies and Ni0 Species to Promote the Stability of a Ni/ZrO_2 Catalyst for Dry Reforming of Methane at Low Temperatures. *ACS Catal.* **2023**, *13*, 6486–6496. [CrossRef]
90. Ruckenstein, E.; Hu, Y.H. Carbon dioxide reforming of methane over nickel/alkaline earth metal oxide catalysts. *Appl. Catal. A Gen.* **1995**, *133*, 149–161. [CrossRef]
91. Zuo, Z.; Liu, S.; Wang, Z.; Liu, C.; Huang, W.; Huang, J.; Liu, P. Dry Reforming of Methane on Single-Site Ni/MgO Catalysts: Importance of Site Confinement. *ACS Catal.* **2018**, *8*, 9821–9835. [CrossRef]
92. Rosdin, R.D.B.; Yusuf, M.; Abdullah, B. Dry reforming of methane over Ni-based catalysts: Effect of ZrO_2 and MgO addition as support. *Mater. Lett. X* **2021**, *12*, 100095. [CrossRef]
93. Bagabas, A.; Al-Fatesh, A.S.; Kasim, S.O.; Arasheed, R.; Ibrahim, A.A.; Ashamari, R.; Anojaidi, K.; Fakeeha, A.H.; Abu-Dahrieh, J.K.; Abasaeed, A.E. Optimizing MgO Content for Boosting γ-Al_2O_3-Supported Ni Catalyst in Dry Reforming of Methane. *Catalysts* **2021**, *11*, 1233. [CrossRef]
94. Zeng, F.; Zhang, J.; Xu, R.; Zhang, R.; Ge, J. Highly dispersed Ni/MgO-mSiO_2 catalysts with excellent activity and stability for dry reforming of methane. *Nano Res.* **2022**, *15*, 5004–5013. [CrossRef]
95. Han, R.; Xing, S.; Wang, Y.; Wei, L.; Li, Z.; Yang, C.; Song, C.; Liu, Q. Two birds with one stone: MgO promoted Ni-CaO as stable and coke-resistant bifunctional materials for integrated CO_2 capture and conversion. *Sep. Purif. Technol.* **2023**, *307*, 122808. [CrossRef]
96. Sun, X.; Wang, Y.; Yan, B. Enhancing Coke Resistance of Mg_1–xNixAl_2O_4 Catalysts for Dry Reforming of Methane via a Doping-Segregation Strategy. *ChemCatChem* **2023**, *15*, e202300220. [CrossRef]
97. Zhang, Y.; Zhang, G.; Liu, J.; Li, T.; Wang, Y.; Zhao, Y.; Li, G.; Zhang, Y. Dry reforming of methane over Ni/SiO_2 catalysts: Role of support structure properties. *Fuel* **2023**, *340*, 127490. [CrossRef]
98. Zhang, Y.; Zhang, G.; Liu, J.; Li, T.; Zhang, X.; Wang, Y.; Zhao, Y.; Li, G.; Zhang, Y. Insight into the role of preparation method on the structure and size effect of Ni/MSS catalysts for dry reforming of methane. *Fuel Process. Technol.* **2023**, *250*, 107891. [CrossRef]
99. Song, Q.; Ran, R.; Wu, X.; Si, Z.; Weng, D. Dry reforming of methane over Ni catalysts supported on micro- and mesoporous silica. *J. CO_2 Util.* **2023**, *68*, 102387. [CrossRef]
100. Chen, S.; Niu, J.; Zheng, X.; Liu, H.; Jin, Y.; Ran, J. Unraveling the effect of particle size of active metals in Ni/MgO on methane activation and carbon growth mechanism. *Phys. Chem. Chem. Phys.* **2024**, *26*, 1255–1266. [CrossRef] [PubMed]
101. Zhang, S.; Cheng, F.; Xie, K. Stable Ni nanocrystals on porous single-crystalline MgO particles for enhanced dry reforming activity and durability of CH_4/CO_2. *Catal. Sci. Technol.* **2024**, *14*, 681–688. [CrossRef]
102. Li, G.; Hao, H.; Jin, P.; Wang, M.; Yu, Y.; Zhang, C. Dry reforming of methane over Ni/Al_2O_3 catalysts: Support morphological effect on the coke resistance. *Fuel* **2024**, *362*, 130855. [CrossRef]
103. Yang, G.S.; Kang, J.; Park, E.D. Aqueous-Phase Partial Oxidation of Methane over Pd−Fe/ZSM-5 with O_2 in the Presence of H_2. *ChemCatChem* **2023**, *15*, e202201630. [CrossRef]
104. Xu, Z.; Kang, J.; Park, E.D. Continuous gas-phase oxidation of methane into methanol over Cu-mordenite. *Microporous Mesoporous Mater.* **2023**, *360*, 112727. [CrossRef]
105. Huang, T.; Huang, W.; Huang, J.; Ji, P. Methane reforming reaction with carbon dioxide over SBA-15 supported Ni–Mo bimetallic catalysts. *Fuel Process. Technol.* **2011**, *92*, 1868–1875. [CrossRef]
106. Aziz, M.A.A.; Jalil, A.A.; Wongsakulphasatch, S.; Vo, D.-V.N. Understanding the role of surface basic sites of catalysts in CO_2 activation in dry reforming of methane: A short review. *Catal. Sci. Technol.* **2020**, *10*, 35–45. [CrossRef]

107. Sumi, T.; Murata, D.; Kitamura, H.; Kubota, S.; Miyake, K.; Uchida, Y.; Miyamoto, M.; Nishiyama, N. Formation of Ni Species Anchored on a Silicalite-1 Zeolite Framework as a Catalyst with High Coke Deposition Resistance on Dry Reforming of Methane. *Cryst. Growth Des.* **2023**, *23*, 3308–3313. [CrossRef]
108. Cheng, Q.; Yao, X.; Ou, L.; Hu, Z.; Zheng, L.; Li, G.; Morlanes, N.; Cerrillo, J.L.; Castaño, P.; Li, X.; et al. Highly Efficient and Stable Methane Dry Reforming Enabled by a Single-Site Cationic Ni Catalyst. *J. Am. Chem. Soc.* **2023**, *145*, 25109–25119. [CrossRef]
109. Zhu, Q.; Liu, Y.; Qin, X.; Liu, L.; Ren, Z.; Tao, X.; Wang, C.; Wang, H.; Li, L.; Liu, X.; et al. Zeolite fixed cobalt–nickel nanoparticles for coking and sintering resistance in dry reforming of methane. *Chem. Eng. Sci.* **2023**, *280*, 119030. [CrossRef]
110. Wang, H.; Wang, L.; Xiao, F.-S. Metal@Zeolite Hybrid Materials for Catalysis. *ACS Cent. Sci.* **2020**, *6*, 1685–1697. [CrossRef] [PubMed]
111. Xu, S.; Slater, T.J.A.; Huang, H.; Zhou, Y.; Jiao, Y.; Parlett, C.M.A.; Guan, S.; Chansai, S.; Xu, S.; Wang, X.; et al. Developing silicalite-1 encapsulated Ni nanoparticles as sintering-/coking-resistant catalysts for dry reforming of methane. *Chem. Eng. J.* **2022**, *446*, 137439. [CrossRef]
112. Fujitsuka, H.; Kobayashi, T.; Tago, T. Development of Silicalite-1-encapsulated Ni nanoparticle catalyst from amorphous silica-coated Ni for dry reforming of methane: Achieving coke formation suppression and high thermal stability. *J. CO_2 Util.* **2021**, *53*, 101707. [CrossRef]
113. Liu, Y.; Chen, Y.; Gao, Z.; Zhang, X.; Zhang, L.; Wang, M.; Chen, B.; Diao, Y.; Li, Y.; Xiao, D.; et al. Embedding high loading and uniform Ni nanoparticles into silicalite-1 zeolite for dry reforming of methane. *Appl. Catal. B Environ.* **2022**, *307*, 121202. [CrossRef]
114. Huang, C.; Zhang, Y.; Han, D.; He, B.; Sun, X.; Liu, M.; Mei, Y.; Zu, Y. Small-sized Ni nanoparticles embedded nickel phyllosilicate as a metal-acid bifunctional zeolite catalyst for cooperatively boosting CO_2-CH_4 reforming. *Fuel* **2023**, *331*, 125957. [CrossRef]
115. Kulkarni, S.R.; Velisoju, V.K.; Tavares, F.; Dikhtiarenko, A.; Gascon, J.; Castaño, P. Silicon carbide in catalysis: From inert bed filler to catalytic support and multifunctional material. *Catal. Rev.* **2023**, *65*, 174–237. [CrossRef]
116. Gunduz Meric, G.; Arbag, H.; Degirmenci, L. Coke minimization via SiC formation in dry reforming of methane conducted in the presence of Ni-based core–shell microsphere catalysts. *Int. J. Hydrogen Energy* **2017**, *42*, 16579–16588. [CrossRef]
117. Zhang, Z.; Zhao, G.; Bi, G.; Guo, Y.; Xie, J. Monolithic SiC-foam supported Ni-La_2O_3 composites for dry reforming of methane with enhanced carbon resistance. *Fuel Process. Technol.* **2021**, *212*, 106627. [CrossRef]
118. Feng, K.; Zhang, J.; Li, Z.; Liu, X.; Pan, Y.; Wu, Z.; Tian, J.; Chen, Y.; Zhang, C.; Xue, Q.; et al. Spontaneous regeneration of active sites against catalyst deactivation. *Appl. Catal. B Environ.* **2024**, *344*, 123647. [CrossRef]
119. Zhang, X.; Shen, Y.; Liu, Y.; Zheng, J.; Deng, J.; Yan, T.; Cheng, D.; Zhang, D. Unraveling the Unique Promotion Effects of a Triple Interface in Ni Catalysts for Methane Dry Reforming. *Ind. Eng. Chem. Res.* **2023**, *62*, 4965–4975. [CrossRef]
120. Zheng, J.; Impeng, S.; Liu, J.; Deng, J.; Zhang, D. Mo promoting Ni-based catalysts confined by halloysite nanotubes for dry reforming of methane: Insight of coking and H_2S poisoning resistance. *Appl. Catal. B Environ.* **2024**, *342*, 123369. [CrossRef]
121. Alli, R.D.; Mahinpey, N. Influence of organic ligand and nickel loading on the performance of MOF-derived catalysts for dry reforming of methane. *Fuel* **2024**, *361*, 130756. [CrossRef]
122. De, S.; Zhang, J.; Luque, R.; Yan, N. Ni-based bimetallic heterogeneous catalysts for energy and environmental applications. *Energy Environ. Sci.* **2016**, *9*, 3314–3347. [CrossRef]
123. Zou, Z.; Zhang, T.; Lv, L.; Tang, W.; Zhang, G.; Kumar Gupta, R.; Wang, Y.; Tang, S. Preparation adjacent Ni-Co bimetallic nano catalyst for dry reforming of methane. *Fuel* **2023**, *343*, 128013. [CrossRef]
124. Palanichamy, K.; Umasankar, S.; Ganesh, S.; Sasirekha, N. Highly coke resistant Ni–Co/KCC-1 catalysts for dry reforming of methane. *Int. J. Hydrogen Energy* **2023**, *48*, 11727–11745. [CrossRef]
125. Duan, X.; Pan, J.; Yang, X.; Wan, C.; Lin, X.; Li, D.; Jiang, L. Nickel–cobalt bimetallic catalysts prepared from hydrotalcite-like compounds for dry reforming of methane. *Int. J. Hydrogen Energy* **2022**, *47*, 24358–24373. [CrossRef]
126. Nataj, S.M.M.; Alavi, S.M.; Mazloom, G. Modeling and optimization of methane dry reforming over Ni–Cu/Al_2O_3 catalyst using Box–Behnken design. *J. Energy Chem.* **2018**, *27*, 1475–1488. [CrossRef]
127. Danghyan, V.; Kumar, A.; Mukasyan, A.; Wolf, E.E. An active and stable NiOMgO solid solution based catalysts prepared by paper assisted combustion synthesis for the dry reforming of methane. *Appl. Catal. B Environ.* **2020**, *273*, 119056. [CrossRef]
128. Zhang, G.; Wang, Y.; Li, X.; Bai, Y.; Zheng, L.; Wu, L.; Han, X. Effect of Gd Promoter on the Structure and Catalytic Performance of Mesoporous Ni/Al_2O_3–CeO_2 in Dry Reforming of Methane. *Ind. Eng. Chem. Res.* **2018**, *57*, 17076–17085. [CrossRef]
129. Sheng, K.; Luan, D.; Jiang, H.; Zeng, F.; Wei, B.; Pang, F.; Ge, J. Ni_xCo_y Nanocatalyst Supported by ZrO_2 Hollow Sphere for Dry Reforming of Methane: Synergetic Catalysis by Ni and Co in Alloy. *ACS Appl. Mater. Interfaces* **2019**, *11*, 24078–24087. [CrossRef]
130. Al-Fatesh, A.S.; Kumar, R.; Kasim, S.O.; Ibrahim, A.A.; Fakeeha, A.H.; Abasaeed, A.E.; Atia, H.; Armbruster, U.; Kreyenschulte, C.; Lund, H.; et al. Effect of Cerium Promoters on an MCM-41-Supported Nickel Catalyst in Dry Reforming of Methane. *Ind. Eng. Chem. Res.* **2022**, *61*, 164–174. [CrossRef]
131. Wang, H.; Dong, X.; Zhao, T.; Yu, H.; Li, M. Dry reforming of methane over bimetallic Ni-Co catalyst prepared from $La(Co_xNi_{1-x})_{0.5}Fe_{0.5}O_3$ perovskite precursor: Catalytic activity and coking resistance. *Appl. Catal. B Environ.* **2019**, *245*, 302–313. [CrossRef]
132. Liang, T.-Y.; Senthil Raja, D.; Chin, K.C.; Huang, C.-L.; Sethupathi, S.A.P.; Leong, L.K.; Tsai, D.-H.; Lu, S.-Y. Bimetallic Metal–Organic Framework-Derived Hybrid Nanostructures as High-Performance Catalysts for Methane Dry Reforming. *ACS Appl. Mater. Interfaces* **2020**, *12*, 15183–15193. [CrossRef] [PubMed]

133. Peng, R.; Chen, Y.; Zhang, B.; Li, Z.; Cui, X.; Guo, C.; Zhao, Y.; Zhang, J. Tailoring the stability of Ni-Fe/mayenite in methane–Carbon dioxide reforming. *Fuel* **2021**, *284*, 118909. [CrossRef]
134. Wan, C.; Song, K.; Pan, J.; Huang, M.; Luo, R.; Li, D.; Jiang, L. Ni–Fe/Mg(Al)O alloy catalyst for carbon dioxide reforming of methane: Influence of reduction temperature and Ni–Fe alloying on coking. *Int. J. Hydrogen Energy* **2020**, *45*, 33574–33585. [CrossRef]
135. Xiao, Z.; Hou, F.; Zhang, J.; Zheng, Q.; Xu, J.; Pan, L.; Wang, L.; Zou, J.; Zhang, X.; Li, G. Methane Dry Reforming by Ni–Cu Nanoalloys Anchored on Periclase-Phase $MgAlO_x$ Nanosheets for Enhanced Syngas Production. *ACS Appl. Mater. Interfaces* **2021**, *13*, 48838–48854. [CrossRef] [PubMed]
136. Sagar, T.V.; Padmakar, D.; Lingaiah, N.; Sai Prasad, P.S. Influence of Solid Solution Formation on the Activity of CeO_2 Supported Ni–Cu Mixed Oxide Catalysts in Dry Reforming of Methane. *Catal. Lett.* **2019**, *149*, 2597–2606. [CrossRef]
137. Zhang, X.; Deng, J.; Pupucevski, M.; Impeng, S.; Yang, B.; Chen, G.; Kuboon, S.; Zhong, Q.; Faungnawakij, K.; Zheng, L.; et al. High-Performance Binary Mo–Ni Catalysts for Efficient Carbon Removal during Carbon Dioxide Reforming of Methane. *ACS Catal.* **2021**, *11*, 12087–12095. [CrossRef]
138. Károlyi, J.; Németh, M.; Evangelisti, C.; Sáfrán, G.; Schay, Z.; Horváth, A.; Somodi, F. Carbon dioxide reforming of methane over Ni–In/SiO_2 catalyst without coke formation. *J. Ind. Eng. Chem.* **2018**, *58*, 189–201. [CrossRef]
139. Araiza, D.G.; Arcos, D.G.; Gómez-Cortés, A.; Díaz, G. Dry reforming of methane over Pt-Ni/CeO_2 catalysts: Effect of the metal composition on the stability. *Catal. Today* **2021**, *360*, 46–54. [CrossRef]
140. Andraos, S.; Abbas-Ghaleb, R.; Chlala, D.; Vita, A.; Italiano, C.; Laganà, M.; Pino, L.; Nakhl, M.; Specchia, S. Production of hydrogen by methane dry reforming over ruthenium-nickel based catalysts deposited on Al_2O_3, $MgAl_2O_4$, and YSZ. *Int. J. Hydrogen Energy* **2019**, *44*, 25706–25716. [CrossRef]
141. García-Diéguez, M.; Pieta, I.S.; Herrera, M.C.; Larrubia, M.A.; Alemany, L.J. RhNi nanocatalysts for the CO_2 and $CO_2 + H_2O$ reforming of methane. *Catal. Today* **2011**, *172*, 136–142. [CrossRef]
142. Mao, Y.; Zhang, L.; Zheng, X.; Liu, W.; Cao, Z.; Peng, H. Coke-resistance over Rh–Ni bimetallic catalyst for low temperature dry reforming of methane. *Int. J. Hydrogen Energy* **2023**, *48*, 13890–13901. [CrossRef]
143. Tang, L.; Huang, X.; Ran, J.; Guo, F.; Niu, J.; Qiu, H.; Ou, Z.; Yan, Y.; Yang, Z.; Qin, C. Density functional theory studies on direct and oxygen assisted activation of C–H bond for dry reforming of methane over Rh–Ni catalyst. *Int. J. Hydrogen Energy* **2022**, *47*, 30391–30403. [CrossRef]
144. Zhou, H.; Zhang, T.; Sui, Z.; Zhu, Y.-A.; Han, C.; Zhu, K.; Zhou, X. A single source method to generate Ru-Ni-MgO catalysts for methane dry reforming and the kinetic effect of Ru on carbon deposition and gasification. *Appl. Catal. B: Environ.* **2018**, *233*, 143–159. [CrossRef]
145. Álvarez, M.A.; Bobadilla, L.F.; Garcilaso, V.; Centeno, M.A.; Odriozola, J.A. CO_2 reforming of methane over Ni-Ru supported catalysts: On the nature of active sites by operando DRIFTS study. *J. CO_2 Util.* **2018**, *24*, 509–515. [CrossRef]
146. Miao, C.; Chen, S.; Shang, K.; Liang, L.; Ouyang, J. Highly Active Ni–Ru Bimetallic Catalyst Integrated with MFI Zeolite-Loaded Cerium Zirconium Oxide for Dry Reforming of Methane. *ACS Appl. Mater. Interfaces* **2022**, *14*, 47616–47632. [CrossRef]
147. Niu, J.; Wang, Y.; Liland, E.S.; Regli, K.S.; Yang, J.; Rout, K.R.; Luo, J.; Rønning, M.; Ran, J.; Chen, D. Unraveling Enhanced Activity, Selectivity, and Coke Resistance of Pt–Ni Bimetallic Clusters in Dry Reforming. *ACS Catal.* **2021**, *11*, 2398–2411. [CrossRef]
148. Wu, Z.; Yang, B.; Miao, S.; Liu, W.; Xie, J.; Lee, S.; Pellin, M.J.; Xiao, D.; Su, D.; Ma, D. Lattice Strained Ni-Co alloy as a High-Performance Catalyst for Catalytic Dry Reforming of Methane. *ACS Catal.* **2019**, *9*, 2693–2700. [CrossRef]
149. Huang, L.; Li, D.; Tian, D.; Jiang, L.; Li, Z.; Wang, H.; Li, K. Optimization of Ni-Based Catalysts for Dry Reforming of Methane via Alloy Design: A Review. *Energy Fuels* **2022**, *36*, 5102–5151. [CrossRef]
150. Horlyck, J.; Lawrey, C.; Lovell, E.C.; Amal, R.; Scott, J. Elucidating the impact of Ni and Co loading on the selectivity of bimetallic NiCo catalysts for dry reforming of methane. *Chem. Eng. J.* **2018**, *352*, 572–580. [CrossRef]
151. Tu, W.; Ghoussoub, M.; Singh, C.V.; Chin, Y.-H.C. Consequences of Surface Oxophilicity of Ni, Ni-Co, and Co Clusters on Methane Activation. *J. Am. Chem. Soc.* **2017**, *139*, 6928–6945. [CrossRef] [PubMed]
152. Turap, Y.; Wang, I.; Fu, T.; Wu, Y.; Wang, Y.; Wang, W. Co–Ni alloy supported on CeO_2 as a bimetallic catalyst for dry reforming of methane. *Int. J. Hydrogen Energy* **2020**, *45*, 6538–6548. [CrossRef]
153. Liu, J.; Zhang, Y.; Liang, Z.; Zhang, G.; Wang, Y.; Zhao, Y.; Li, G.; Lv, Y. Enhancing the dry reforming of methane over Ni-Co-Y/WC-AC catalyst: Influence of the different Ni/Co ratio on the catalytic performance. *Fuel* **2023**, *335*, 127082. [CrossRef]
154. Kumari, R.; Sengupta, S. Catalytic CO_2 reforming of CH_4 over $MgAl_2O_4$ supported Ni-Co catalysts for the syngas production. *Int. J. Hydrogen Energy* **2020**, *45*, 22775–22787. [CrossRef]
155. Shakir, M.; Prasad, M.; Ray, K.; Sengupta, S.; Sinhamahapatra, A.; Liu, S.; Vuthaluru, H.B. $NaBH_4$-Assisted Synthesis of B–(Ni–Co)/$MgAl_2O_4$ Nanostructures for the Catalytic Dry Reforming of Methane. *ACS Appl. Nano Mater.* **2022**, *5*, 10951–10961. [CrossRef]
156. Chen, X.; Yin, L.; Long, K.; Sun, H.; Sun, M.; Wang, H.; Zhang, Q.; Ning, P. The reconstruction of Ni particles on SBA-15 by thermal activation for dry reforming of methane with excellent resistant to carbon deposition. *J. Energy Inst.* **2020**, *93*, 2255–2263. [CrossRef]
157. Zhang, J.; Wang, H.; Dalai, A.K. Effects of metal content on activity and stability of Ni-Co bimetallic catalysts for CO_2 reforming of CH_4. *Appl. Catal. A Gen.* **2008**, *339*, 121–129. [CrossRef]

158. Chen, S.; Yang, B. Activity and stability of alloyed NiCo catalyst for the dry reforming of methane: A combined DFT and microkinetic modeling study. *Catal. Today* **2022**, *400–401*, 59–65. [CrossRef]
159. Ou, Z.; Ran, J.; Qiu, H.; Huang, X.; Qin, C. Understanding the role of Co segregation on the carbon deposition over Ni–Co bimetal catalyst in dry reforming of methane. *Sep. Purif. Technol.* **2024**, *333*, 125868. [CrossRef]
160. Liu, K.; Xing, F.; Xiao, Y.; Yan, N.; Shimizu, K.-I.; Furukawa, S. Development of a Highly Stable Ternary Alloy Catalyst for Dry Reforming of Methane. *ACS Catal.* **2023**, *13*, 3541–3548. [CrossRef]
161. Li, B.; Yuan, X.; Li, L.; Wang, X.; Li, B. Stabilizing Ni-Co Alloy on Bimodal Mesoporous Alumina to Enhance Carbon Resistance for Dry Reforming of Methane. *Ind. Eng. Chem. Res.* **2021**, *60*, 16874–16886. [CrossRef]
162. Gai, X.; Yang, D.; Tang, R.; Luo, M.; Lu, P.; Xing, C.; Yang, R.; Ma, Q.; Li, Y. Preparation of Ni-Co/SiO_2 catalyst by ammonia reflux impregnation and its CH_4-CO_2 reforming reaction performance. *Fuel* **2022**, *316*, 123337. [CrossRef]
163. Kuboon, S.; Deng, J.; Gao, M.; Faungnawakij, K.; Hasegawa, J.-Y.; Zhang, X.; Shi, L.; Zhang, D. Unraveling the promotional effects of NiCo catalysts over defective boron nitride nanosheets in dry reforming of methane. *Catal. Today* **2022**, *402*, 283–291. [CrossRef]
164. Panda, S.; Joshi, V.; Shrivastaw, V.K.; Das, S.; Poddar, M.; Bal, R.; Bordoloi, A. Enhanced coke-resistant Co-modified Ni/modified alumina catalyst for the bireforming of methane. *Catal. Sci. Technol.* **2023**, *13*, 4506–4516. [CrossRef]
165. Huang, J.; Jones, A.; Waite, T.D.; Chen, Y.; Huang, X.; Rosso, K.M.; Kappler, A.; Mansor, M.; Tratnyek, P.G.; Zhang, H. Fe(II) Redox Chemistry in the Environment. *Chem. Rev.* **2021**, *121*, 8161–8233. [CrossRef]
166. Theofanidis, S.A.; Galvita, V.V.; Poelman, H.; Marin, G.B. Enhanced Carbon-Resistant Dry Reforming Fe-Ni Catalyst: Role of Fe. *ACS Catal.* **2015**, *5*, 3028–3039. [CrossRef]
167. Kim, S.M.; Abdala, P.M.; Margossian, T.; Hosseini, D.; Foppa, L.; Armutlulu, A.; van Beek, W.; Comas-Vives, A.; Copéret, C.; Müller, C. Cooperativity and Dynamics Increase the Performance of NiFe Dry Reforming Catalysts. *J. Am. Chem. Soc.* **2017**, *139*, 1937–1949. [CrossRef]
168. Song, Z.; Wang, Q.; Guo, C.; Li, S.; Yan, W.; Jiao, W.; Qiu, L.; Yan, X.; Li, R. Improved Effect of Fe on the Stable NiFe/Al_2O_3 Catalyst in Low-Temperature Dry Reforming of Methane. *Ind. Eng. Chem. Res.* **2020**, *59*, 17250–17258. [CrossRef]
169. Margossian, T.; Larmier, K.; Kim, S.M.; Krumeich, F.; Müller, C.; Copéret, C. Supported Bimetallic NiFe Nanoparticles through Colloid Synthesis for Improved Dry Reforming Performance. *ACS Catal.* **2017**, *7*, 6942–6948. [CrossRef]
170. Li, Y.; Wang, Q.; Cao, M.; Li, S.; Song, Z.; Qiu, L.; Yu, F.; Li, R.; Yan, X. Structural evolution of robust Ni_3Fe_1 alloy on Al_2O_3 in dry reforming of methane: Effect of iron-surplus strategy from Ni_1Fe_1 to Ni_3Fe_1. *Appl. Catal. B: Environ.* **2023**, *331*, 122669. [CrossRef]
171. Huang, L.; Ma, Y.; Niu, M.; Ren, S.; Guo, Q.; Xu, C.; Shen, B. Formation of H_2O in the CH_4-CO_2 dry reforming process and its activation to this reaction over Ni-Fe/$MC_{12}A_7$ catalysts. *Appl. Catal. B Environ.* **2023**, *334*, 122822. [CrossRef]
172. Zhang, T.; Liu, Z.; Zhu, Y.-A.; Liu, Z.; Sui, Z.; Zhu, K.; Zhou, X. Dry reforming of methane on Ni-Fe-MgO catalysts: Influence of Fe on carbon-resistant property and kinetics. *Appl. Catal. B Environ.* **2020**, *264*, 118497. [CrossRef]
173. Gaillard, M.; Virginie, M.; Khodakov, A.Y. New molybdenum-based catalysts for dry reforming of methane in presence of sulfur: A promising way for biogas valorization. *Catal. Today* **2017**, *289*, 143–150. [CrossRef]
174. Chen, L.; Xu, Q. Fewer defects, better catalysis? *Science* **2020**, *367*, 737. [CrossRef]
175. Yao, L.; Galvez, M.E.; Hu, C.; Da Costa, P. Mo-promoted Ni/Al_2O_3 catalyst for dry reforming of methane. *Int. J. Hydrogen Energy* **2017**, *42*, 23500–23507. [CrossRef]
176. Abdel Karim Aramouni, N.; Zeaiter, J.; Kwapinski, W.; Leahy, J.J.; Ahmad, M.N. Molybdenum and nickel-molybdenum nitride catalysts supported on MgO-Al_2O_3 for the dry reforming of methane. *J. CO_2 Util.* **2021**, *44*, 101411. [CrossRef]
177. Tang, J.; Meng, J.; Pan, W.; Gu, T.; Zhang, Q.; Zhang, J.; Wang, X.; Bu, C.; Piao, G. Effect of hydroxyl and Mo doping on activity and carbon deposition resistance of hydroxyapatite supported Ni_xMo_y catalyst for syngas production via DRM reaction. *Int. J. Hydrogen Energy* **2023**, *48*, 19033–19045. [CrossRef]
178. Wang, W.-Y.; Liu, J.-H.; Lv, C.-Q.; Ren, R.-R.; Wang, G.-C. Dry reforming of methane on Ni(111) surface with different Mo doping ratio: DFT-assisted microkinetic study. *Appl. Surf. Sci.* **2022**, *581*, 152310. [CrossRef]
179. Song, K.; Lu, M.; Xu, S.; Chen, C.; Zhan, Y.; Li, D.; Au, C.; Jiang, L.; Tomishige, K. Effect of alloy composition on catalytic performance and coke-resistance property of Ni-Cu/Mg(Al)O catalysts for dry reforming of methane. *Appl. Catal. B: Environ.* **2018**, *239*, 324–333. [CrossRef]
180. Han, K.; Wang, S.; Liu, Q.; Wang, F. Optimizing the Ni/Cu Ratio in Ni–Cu Nanoparticle Catalysts for Methane Dry Reforming. *ACS Appl. Nano Mater.* **2021**, *4*, 5340–5348. [CrossRef]
181. Chatla, A.; Ghouri, M.M.; El Hassan, O.W.; Mohamed, N.; Prakash, A.V.; Elbashir, N.O. An experimental and first principles DFT investigation on the effect of Cu addition to Ni/Al_2O_3 catalyst for the dry reforming of methane. *Appl. Catal. A: Gen.* **2020**, *602*, 117699. [CrossRef]
182. Yang, Y.; Lin, Y.-A.; Yan, X.; Chen, F.; Shen, Q.; Zhang, L.; Yan, N. Cooperative Atom Motion in Ni–Cu Nanoparticles during the Structural Evolution and the Implication in the High-Temperature Catalyst Design. *ACS Appl. Energy Mater.* **2019**, *2*, 8894–8902. [CrossRef]
183. Bekheet, M.F.; Delir Kheyrollahi Nezhad, P.; Bonmassar, N.; Schlicker, L.; Gili, A.; Praetz, S.; Gurlo, A.; Doran, A.; Gao, Y.; Heggen, M.; et al. Steering the Methane Dry Reforming Reactivity of Ni/La_2O_3 Catalysts by Controlled In Situ Decomposition of Doped La_2NiO_4 Precursor Structures. *ACS Catal.* **2021**, *11*, 43–59. [CrossRef]
184. Wang, F.; Han, B.; Zhang, L.; Xu, L.; Yu, H.; Shi, W. CO_2 reforming with methane over small-sized Ni@SiO_2 catalysts with unique features of sintering-free and low carbon. *Appl. Catal. B Environ.* **2018**, *235*, 26–35. [CrossRef]

185. Zhao, Y.; Li, H.; Li, H. NiCo@SiO_2 core-shell catalyst with high activity and long lifetime for CO_2 conversion through DRM reaction. *Nano Energy* **2018**, *45*, 101–108. [CrossRef]
186. Pang, Y.; Dou, Y.; Zhong, A.; Jiang, W.; Gu, L.; Feng, X.; Ji, W.; Au, C.-T. Nanostructured Ru-Co@SiO_2: Highly efficient yet durable for CO_2 reforming of methane with a desirable H_2/CO ratio. *Appl. Catal. A Gen.* **2018**, *555*, 27–35. [CrossRef]
187. Liu, W.; Li, L.; Zhang, X.; Wang, Z.; Wang, X.; Peng, H. Design of Ni-ZrO_2@SiO_2 catalyst with ultra-high sintering and coking resistance for dry reforming of methane to prepare syngas. *J. CO_2 Util.* **2018**, *27*, 297–307. [CrossRef]
188. Lu, Y.; Guo, D.; Ruan, Y.; Zhao, Y.; Wang, S.; Ma, X. Facile one-pot synthesis of Ni@HSS as a novel yolk-shell structure catalyst for dry reforming of methane. *J. CO_2 Util.* **2018**, *24*, 190–199. [CrossRef]
189. Li, Z.; Jiang, B.; Wang, Z.; Kawi, S. High carbon resistant Ni@Ni phyllosilicate@SiO_2 core shell hollow sphere catalysts for low temperature CH_4 dry reforming. *J. CO_2 Util.* **2018**, *27*, 238–246. [CrossRef]
190. Wang, Y.; Fang, Q.; Shen, W.; Zhu, Z.; Fang, Y. (Ni/$MgAl_2O_4$)@SiO_2 core–shell catalyst with high coke-resistance for the dry reforming of methane. *React. Kinet. Mech. Catal.* **2018**, *125*, 127–139. [CrossRef]
191. Dou, J.; Zhang, R.; Hao, X.; Bao, Z.; Wu, T.; Wang, B.; Yu, F. Sandwiched SiO_2@Ni@ZrO_2 as a coke resistant nanocatalyst for dry reforming of methane. *Appl. Catal. B: Environ.* **2019**, *254*, 612–623. [CrossRef]
192. Zhao, Y.; Kang, Y.; Li, H.; Li, H. CO_2 conversion to synthesis gas via DRM on the durable Al_2O_3/Ni/Al_2O_3 sandwich catalyst with high activity and stability. *Green Chem.* **2018**, *20*, 2781–2787. [CrossRef]
193. Das, S.; Ashok, J.; Bian, Z.; Dewangan, N.; Wai, M.H.; Du, Y.; Borgna, A.; Hidajat, K.; Kawi, S. Silica–Ceria sandwiched Ni core–shell catalyst for low temperature dry reforming of biogas: Coke resistance and mechanistic insights. *Appl. Catal. B Environ.* **2018**, *230*, 220–236. [CrossRef]
194. Kaviani, M.; Rezaei, M.; Mehdi Alavi, S.; Akbari, E. High coke resistance Ni-SiO_2@SiO_2 core-shell catalyst for biogas dry reforming: Effects of Ni loading and calcination temperature. *Fuel* **2022**, *330*, 125609. [CrossRef]
195. Wang, C.; Wu, H.; Jie, X.; Zhang, X.; Zhao, Y.; Yao, B.; Xiao, T. Yolk–Shell Nanocapsule Catalysts as Nanoreactors with Various Shell Structures and Their Diffusion Effect on the CO_2 Reforming of Methane. *ACS Appl. Mater. Interfaces* **2021**, *13*, 31699–31709. [CrossRef] [PubMed]
196. Kim, S.; Lauterbach, J.; Sasmaz, E. Yolk–Shell Pt-NiCe@SiO_2 Single-Atom-Alloy Catalysts for Low-Temperature Dry Reforming of Methane. *ACS Catal.* **2021**, *11*, 8247–8260. [CrossRef]
197. Liu, W.; Li, L.; Lin, S.; Luo, Y.; Bao, Z.; Mao, Y.; Li, K.; Wu, D.; Peng, H. Confined Ni-In intermetallic alloy nanocatalyst with excellent coking resistance for methane dry reforming. *J. Energy Chem.* **2022**, *65*, 34–47. [CrossRef]
198. Lu, Y.; Guo, D.; Zhao, Y.; Zhao, Y.; Wang, S.; Ma, X. Enhanced performance of xNi@yMo-HSS catalysts for DRM reaction via the formation of a novel $SiMoO_x$ species. *Appl. Catal. B: Environ.* **2021**, *291*, 120075. [CrossRef]
199. Shi, Y.; Han, K.; Wang, F. Ni–Cu Alloy Nanoparticles Confined by Physical Encapsulation with SiO_2 and Chemical Metal–Support Interaction with CeO_2 for Methane Dry Reforming. *Inorg. Chem.* **2022**, *61*, 15619–15628. [CrossRef]
200. Lu, Y.; Guo, D.; Zhao, Y.; Moyo, P.S.; Zhao, Y.; Wang, S.; Ma, X. Confined high dispersion of Ni nanoparticles derived from nickel phyllosilicate structure in silicalite-2 shell for dry reforming of methane with enhanced performance. *Microporous Mesoporous Mater.* **2021**, *313*, 110842. [CrossRef]
201. Qu, H.; Yang, H.; Han, L.; He, S.; Liu, J.; Hu, R.; Su, H.; Su, Y. Sandwich-structured nickel/kaolinite catalyst with boosted stability for dry reforming of methane with carbon dioxide. *Chem. Eng. J.* **2023**, *453*, 139694. [CrossRef]
202. Zhang, Q.; Lee, I.; Joo, J.B.; Zaera, F.; Yin, Y. Core–Shell Nanostructured Catalysts. *Acc. Chem. Res.* **2013**, *46*, 1816–1824. [CrossRef] [PubMed]
203. Gawande, M.B.; Goswami, A.; Asefa, T.; Guo, H.; Biradar, A.V.; Peng, D.-L.; Zboril, R.; Varma, R.S. Core–shell nanoparticles: Synthesis and applications in catalysis and electrocatalysis. *Chem. Soc. Rev.* **2015**, *44*, 7540–7590. [CrossRef] [PubMed]
204. Das, S.; Pérez-Ramírez, J.; Gong, J.; Dewangan, N.; Hidajat, K.; Gates, B.C.; Kawi, S. Core–shell structured catalysts for thermocatalytic, photocatalytic, and electrocatalytic conversion of CO_2. *Chem. Soc. Rev.* **2020**, *49*, 2937–3004. [CrossRef] [PubMed]
205. Ghosh Chaudhuri, R.; Paria, S. Core/Shell Nanoparticles: Classes, Properties, Synthesis Mechanisms, Characterization, and Applications. *Chem. Rev.* **2012**, *112*, 2373–2433. [CrossRef] [PubMed]
206. Zhang, J.; Li, F. Coke-resistant Ni@SiO_2 catalyst for dry reforming of methane. *Appl. Catal. B Environ.* **2015**, *176-177*, 513–521. [CrossRef]
207. Park, K.S.; Kwon, J.H.; Yu, J.S.; Jeong, S.Y.; Jo, D.H.; Chung, C.-H.; Bae, J.W. Catalytically stable monodispersed multi-core Ni-Co nanoparticles encapsulated with SiO_2 shells for dry reforming of CH_4 with CO_2. *J. CO_2 Util.* **2022**, *60*, 101984. [CrossRef]
208. Lin, S.; Wang, J.; Mi, Y.; Yang, S.; Wang, Z.; Liu, W.; Wu, D.; Peng, H. Trifunctional strategy for the design and synthesis of a Ni-CeO_2@SiO_2 catalyst with remarkable low-temperature sintering and coking resistance for methane dry reforming. *Chin. J. Catal.* **2021**, *42*, 1808–1820. [CrossRef]
209. Das, S.; Lim, K.H.; Gani, T.Z.H.; Aksari, S.; Kawi, S. Bi-functional CeO_2 coated NiCo-MgAl core-shell catalyst with high activity and resistance to coke and H_2S poisoning in methane dry reforming. *Appl. Catal. B Environ.* **2023**, *323*, 122141. [CrossRef]
210. Han, K.; Wang, S.; Hu, N.; Shi, W.; Wang, F. Alloying Ni–Cu Nanoparticles Encapsulated in SiO_2 Nanospheres for Synergistic Catalysts in CO_2 Reforming with Methane Reaction. *ACS Appl. Mater. Interfaces* **2022**, *14*, 23487–23495. [CrossRef]
211. Kosari, M.; Askari, S.; Seayad, A.M.; Xi, S.; Kawi, S.; Borgna, A.; Zeng, H.C. Strong coke-resistivity of spherical hollow Ni/SiO_2 catalysts with shell-confined high-content Ni nanoparticles for methane dry reforming with CO_2. *Appl. Catal. B: Environ.* **2022**, *310*, 121360. [CrossRef]

212. Singh, S.; Zubenko, D.; Rosen, B.A. Influence of $LaNiO_3$ Shape on Its Solid-Phase Crystallization into Coke-Free Reforming Catalysts. *ACS Catal.* **2016**, *6*, 4199–4205. [CrossRef]
213. Zhao, H.; Zhang, W.; Song, H.; Zhao, J.; Yang, J.; Yan, L.; Qiao, B.; Chou, L. Highly coke-resistant Ni-$La_2O_2CO_3$ catalyst with low Ni loading for dry reforming of methane with carbon dioxide. *Catal. Today* **2022**, *402*, 189–201. [CrossRef]
214. Moogi, S.; Hyun Ko, C.; Hoon Rhee, G.; Jeon, B.-H.; Ali Khan, M.; Park, Y.-K. Influence of catalyst synthesis methods on anti-coking strength of perovskites derived catalysts in biogas dry reforming for syngas production. *Chem. Eng. J.* **2022**, *437*, 135348. [CrossRef]
215. Rabelo-Neto, R.C.; Sales, H.B.E.; Inocêncio, C.V.M.; Varga, E.; Oszko, A.; Erdohelyi, A.; Noronha, F.B.; Mattos, L.V. CO_2 reforming of methane over supported $LaNiO_3$ perovskite-type oxides. *Appl. Catal. B Environ.* **2018**, *221*, 349–361. [CrossRef]
216. Bonmassar, N.; Bekheet, M.F.; Schlicker, L.; Gili, A.; Gurlo, A.; Doran, A.; Gao, Y.; Heggen, M.; Bernardi, J.; Klötzer, B.; et al. In Situ-Determined Catalytically Active State of $LaNiO_3$ in Methane Dry Reforming. *ACS Catal.* **2020**, *10*, 1102–1112. [CrossRef]
217. Kim, W.Y.; Jang, J.S.; Ra, E.C.; Kim, K.Y.; Kim, E.H.; Lee, J.S. Reduced perovskite $LaNiO_3$ catalysts modified with Co and Mn for low coke formation in dry reforming of methane. *Appl. Catal. A Gen.* **2019**, *575*, 198–203. [CrossRef]
218. Shahnazi, A.; Firoozi, S. Improving the catalytic performance of $LaNiO_3$ perovskite by manganese substitution via ultrasonic spray pyrolysis for dry reforming of methane. *J. CO_2 Util.* **2021**, *45*, 101455. [CrossRef]
219. Shahnazi, A.; Firoozi, S. Mesoporous $LaNi_{1\text{-}x}Mn_xO_3$ perovskite with enhanced catalytic performance and coke resistance synthesized via glycine-assisted spray pyrolysis for methane dry reforming. *Mol. Catal.* **2023**, *547*, 113320. [CrossRef]
220. Yadav, P.K.; Das, T. Production of syngas from carbon dioxide reforming of methane by using $LaNi_xFe_{1-x}O_3$ perovskite type catalysts. *Int. J. Hydrogen Energy* **2019**, *44*, 1659–1670. [CrossRef]
221. Iftikhar, S.; Martin, W.; Gao, Y.; Yu, X.; Wang, I.; Wu, Z.; Li, F. $LaNi_xFe_{1-x}O_3$ as flexible oxygen or carbon carriers for tunable syngas production and CO_2 utilization. *Catal. Today* **2023**, *416*, 113854. [CrossRef]
222. Yao, X.; Cheng, Q.; Attada, Y.; Ould-Chikh, S.; Ramírez, A.; Bai, X.; Mohamed, H.O.; Li, G.; Shterk, G.; Zheng, L.; et al. Atypical stability of exsolved Ni-Fe alloy nanoparticles on double layered perovskite for CO_2 dry reforming of methane. *Appl. Catal. B Environ.* **2023**, *328*, 122479. [CrossRef]
223. Das, S.; Bhattar, S.; Liu, L.; Wang, Z.; Xi, S.; Spivey, J.J.; Kawi, S. Effect of Partial Fe Substitution in $La_{0.9}Sr_{0.1}NiO_3$ Perovskite-Derived Catalysts on the Reaction Mechanism of Methane Dry Reforming. *ACS Catal.* **2020**, *10*, 12466–12486. [CrossRef]
224. Bai, J.; Fu, Y.; Kong, W.; Pan, B.; Yuan, C.; Li, S.; Wang, J.; Zhang, J.; Sun, Y. Design of Ni-substituted $La_2(CeZrNi)_2O_7$ Pyrochlore Catalysts for Methane Dry Reforming. *ChemNanoMat* **2022**, *8*, e202100422. [CrossRef]
225. Chai, Y.; Fu, Y.; Feng, H.; Kong, W.; Yuan, C.; Pan, B.; Zhang, J.; Sun, Y. A Nickel-Based Perovskite Catalyst with a Bimodal Size Distribution of Nickel Particles for Dry Reforming of Methane. *ChemCatChem* **2018**, *10*, 2078–2086. [CrossRef]
226. Wei, T.; Qiu, P.; Jia, L.; Tan, Y.; Yang, X.; Sun, S.; Chen, F.; Li, J. Power and carbon monoxide co-production by a proton-conducting solid oxide fuel cell with $La_{0.6}Sr_{0.2}Cr_{0.85}Ni_{0.15}O_{3-\delta}$ for on-cell dry reforming of CH_4 by CO_2. *J. Mater. Chem. A* **2020**, *8*, 9806–9812. [CrossRef]
227. Dama, S.; Ghodke, S.R.; Bobade, R.; Gurav, H.R.; Chilukuri, S. Active and durable alkaline earth metal substituted perovskite catalysts for dry reforming of methane. *Appl. Catal. B Environ.* **2018**, *224*, 146–158. [CrossRef]
228. Peng, W.; Li, Z.; Liu, B.; Qiu, P.; Yan, D.; Jia, L.; Li, J. Enhanced activity and stability of Ce-doped $PrCrO_3$-supported nickel catalyst for dry reforming of methane. *Sep. Purif. Technol.* **2022**, *303*, 122245. [CrossRef]
229. Chen, C.; Wei, J.; Lu, Y.; Duyar, M.S.; Huang, Y.; Lin, L.; Ye, R. Confinement effects over Ni-based catalysts for methane dry reforming. *Catal. Sci. Technol.* **2023**, *13*, 6089–6101. [CrossRef]
230. Bian, Z.; Kawi, S. Sandwich-like silica@ Ni@ silica multicore–shell catalyst for the low-temperature dry reforming of methane: Confinement effect against carbon formation. *ChemCatChem* **2018**, *10*, 320–328. [CrossRef]
231. Kim, D.H.; Seo, J.-C.; Kim, Y.J.; Kim, J.; Yoon, S.; Ra, H.; Kim, M.-J.; Lee, K. Ni-Co alloy catalyst derived from $Ni_xCo_y/MgAl_2O_4$ via exsolution method for high coke resistance toward dry reforming of methane. *Catal. Today* **2024**, *425*, 114337. [CrossRef]
232. Roh, J.; Park, H.; Kwon, H.; Joo, C.; Moon, I.; Cho, H.; Ro, I.; Kim, J. Interpretable machine learning framework for catalyst performance prediction and validation with dry reforming of methane. *Appl. Catal. B Environ.* **2024**, *343*, 123454. [CrossRef]
233. Alotaibi, F.N.; Berrouk, A.S.; Saeed, M. Optimization of Yield and Conversion Rates in Methane Dry Reforming Using Artificial Neural Networks and the Multiobjective Genetic Algorithm. *Ind. Eng. Chem. Res.* **2023**, *62*, 17084–17099. [CrossRef]
234. Yoon, Y.; You, H.M.; Kim, H.J.; Curnan, M.T.; Kim, K.; Han, J.W. Computational Catalyst Design for Dry Reforming of Methane: A Review. *Energy Fuels* **2022**, *36*, 9844–9865. [CrossRef]
235. Lei, Y.; Ye, J.; García-Antón, J.; Liu, H. Recent advances in the built-in electric-field-assisted photocatalytic dry reforming of methane. *Chin. J. Catal.* **2023**, *53*, 72–101. [CrossRef]
236. Malik, M.I.; Achouri, I.E.; Abatzoglou, N.; Gitzhofer, F. Intensified performance of methane dry reforming based on non-thermal plasma technology: Recent progress and key challenges. *Fuel Process. Technol.* **2023**, *245*, 107748. [CrossRef]
237. Zheng, L.; Ambrosetti, M.; Tronconi, E. Joule-Heated Catalytic Reactors toward Decarbonization and Process Intensification: A Review. *ACS Eng. Au* **2024**, *4*, 4–21. [CrossRef]